Submitted to *Journal of the European Ceramic Society*, January 2019; Revised March 2019

Fabricating toughened super-hard B_4C composites at lower temperature by transient liquid-phase assisted spark plasma sintering with $MoSi_2$ additives

Cristina Ojalvo, Fernando Guiberteau, Angel L. Ortiz*

Departamento de Ingeniería Mecánica, Energética y de los Materiales,

Universidad de Extremadura, 06006 Badajoz, Spain.

Abstract

Toughened, super-hard B_4C triplex-particulate composites were densified by spark plasma sintering with $MoSi_2$ additives (5, 10, and 15 vol.%) at temperatures in the range 1750-1850 °C at which the reference monolithic B_4C ceramics are porous. It is proved that $MoSi_2$ is a reactive sintering additive that promotes densification by transient liquid-phase sintering, thus yielding fully-dense B_4C-MoB_2-SiC composites at relatively lower temperatures. Specifically, the $MoSi_2$ first reacts at moderate temperatures (<1150 °C) with part of B_4C to form MoB_2, SiC, and Si. This last is a transient component that eventually melts (at ~1400 °C), contributing to densification by liquid-phase sintering, and then (at 1500-1700 °C) reacts with free C present in the B_4C starting powders to form more SiC, after which densification continues by solid-state sintering. It is found that these B_4C-MoB_2-SiC composites are super-hard (~30 GPa), tough (~3-4 $MPa{\cdot}m^{1/2}$), and fine-grained, a combination that renders them very appealing for structural applications. Finally, research opportunities are discussed for the future microstructural design of a novel family of toughened, ultra-hard/super-hard multi-particulate composites based on B_4C plus refractory borides and carbides.

Keywords: B_4C; super-hard ceramic composites; spark-plasma sintering; sintering additives; mechanical properties.

* Corresponding author:

Angel L. Ortiz
Phone: +34 924289600 Ext: 86726
Fax: +34 924289601
E-mail: **alortiz@unex.es**

1. Introduction

There is growing demand for super-hard monolithic ceramics and ceramic composites for use in a myriad of structural applications requiring great resistance to contact damage, both without and with friction. Examples of such applications are armours for the protection of personnel and vehicles against ballistic projectiles, components for industrial machinery (dies, bearings, seals, valves, nozzles, etc.), and machining/cutting tools (drills, end mills, reamers, blades, wheels, etc.), to name but a few. Unfortunately however, the current list of super-hard ceramics (i.e., with hardness ideally above 30 GPa under Vickers indentation) is very short [1], and is limited basically to diamond [2-4], B_4C [5,6], and a few nitrides (i.e., BN, C_3N_4, and BC_2N) [2-3,7-9], borides (i.e., OsB_2, ReB_2, and WB_2) [10,11], and oxides (i.e., B_6O) [12,13]. Of these, B_4C receives most attention because diamond is prohibitively expensive and the rest are very exotic. In addition, B_4C is ultra-lightweight (i.e., ~2.52 g/cm^3 density), which is always very desirable in any engineering application but essential in many of them (armour, rotating/moving tribocomponents, etc.). Moreover, B_4C is ultra-refractory (i.e., ~2450 °C melting point) too, and therefore appealing for high-temperature engineering applications.

The bane of B_4C is, as for the rest of the ultra-refractory ceramics, its poor sinterability [14]. This is due to the strong covalent bonding and low self-diffusion coefficients imposing serious kinetic restrictions, and to the oxide impurities promoting coarsening over densification [15-17]. It is then quite common to circumvent this problem by using densification aids [5,14]. Which one is chosen is not a trivial decision, however, because they all have their own advantages and drawbacks. Overall, solid-state-sintered B_4C ceramics are harder and more refractory, but are brittle and have coarse-grained microstructures undesirable in terms of strength and wear resistance. Liquid-phase-sintered B_4C ceramics have fine-grained

microstructures, and are stronger and tougher, but the residual intergranular phase limits their hardness and refractoriness. This dichotomy could be avoided by using so-called transient liquid-phase sintering,[I] which exploits the benefits of both liquid-phase sintering and solid-state sintering. This enticing approach has recently been applied to B_4C, in particular using metallic and intermetallic sintering additives [18,19].

Given its ultra-high refractoriness, sintering additives suitable for B_4C could be those already used successfully for densifying ultra-high-temperature ceramics (UHTCs)[II] [20]. Of these, there stands out $MoSi_2$, which is regularly used for carbide-based UHTCs [21-29]. Its great appeal is that it also strengthens and toughens UHTCs, and provides them with superior oxidation resistance. Unsurprisingly, $MoSi_2$ has already been used to fabricate super-coarse-grained, dense B_4C composites by hot-pressing [30]. Interestingly, the hot-pressing conditions used were relatively smooth (for B_4C), and resulted in super-hard, tougher B_4C composites. That study raised various questions of great interest, namely: (*i*) can $MoSi_2$ also be used to densify fine-grained B_4C composites by ultra-fast sintering (spark plasma sintering (SPS)[III] in particular)?; (*ii*) if so, what is the mechanism of this sintering?; and (*iii*) how does the $MoSi_2$ addition affect the densification kinetics and the mechanical properties of these composites? In the present study we shall answer these questions, with the expectation that the scientific

[I] In transient liquid-phase sintering, the sintering aids first melt at an early stage of sintering, and then that liquid reacts with the solid, disappearing as sintering proceeds further.

[II] UHTCs are a family of super-refractory ceramics (ideally with melting points above 3000 °C) based on borides, carbides, and nitrides of the early-transition metals.

[III] SPS is currently the best exponent of ultra-fast sintering techniques. It uses much shorter densification cycles than either hot-pressing or conventional pressureless sintering (i.e., heating/cooling ramps are one order of magnitude faster (hundreds vs tens of °C/min), and holding times are one order of magnitude shorter (min vs h)). SPS essentially lies in the repeated application of high energy, low voltage, pulsed direct electrical current under mechanical pressure, and is then an electric current-assisted sintering technique of low electric field (only a few V/cm).

knowledge gained may contribute to guiding the future fabrication of novel B_4C composites for engineering applications.

2. Experimental Procedure

The starting powders, obtained from a commercial source (H.C. Starck, Germany) and used in their as-received condition, were B_4C (Grade HD20; d_{50} ~0.3-0.6 µm) and $MoSi_2$ (Grade B; d_{50} ~3.5-5 µm). According to the manufacturer's specifications, the B_4C powder has a B:C atom ratio of 3.8, and the following mass fractions (in %): C 22.0, N 0.3, O 1.8, Si 0.09, Al 0.01. The corresponding data for the $MoSi_2$ are: Si 36.7, C 0.06, O 0.52, and N 0.02. Consequently, the B_4C powder contains free C, and the $MoSi_2$ powder does not contain residual Si. Three powder batches were prepared having B_4C-$MoSi_2$ relative compositions of 95-5 vol.%, 90-10 vol.%, and 85-15 vol.%. To this end, the B_4C and $MoSi_2$ powders were first combined in appropriate proportions in wt.%, then mixed/homogenized by wet ball-milling in methanol for 24 h, dried on a hot-plate while stirring, and finally de-agglomerated by crushing.

Next, the as-received B_4C powder and these three B_4C-$MoSi_2$ powder mixtures were loaded into graphite dies (2-cm diameter) lined with graphite foil and covered by graphite blankets, and were SPS-ed (HP-D-10, FCT Systeme GmbH, Germany) in dynamic vacuum. The common SPS conditions were 100 °C/min heating, 50 MPa pressure, and 5 min soaking, whereas the target temperature was varied in the range 1700-1850 °C. The SPS furnace is equipped with an axial optical pyrometer that measures the temperature on a hole machined across the upper graphite punch, and therefore these temperatures are not directly comparable with those measured by others in SPS furnaces equipped with radial optical pyrometers focused on the graphite die. Except for the ultra-fast sintering cycle, these SPS conditions are similar to those

used in the earlier hot-pressing study (i.e., 1700-1900 °C for 2 h under 30-50 MPa). Table 1 lists the particular conditions used in each case. Given that the expectation is that $MoSi_2$ would facilitate the densification, lower target SPS temperatures were tested for the powder mixtures with 10 or 15 vol.% $MoSi_2$. The as-received B_4C powder is the baseline reference for comparison, and therefore was consolidated at all target SPS temperatures. During each SPS cycle the shrinkage curve was logged, then corrected for the expansion of the graphite parts, and converted to a densification curve for subsequent analysis.

The resulting monolithic ceramics and ceramic composites were ground and polished to a 1-μm finish, and also intentionally broken. They were characterized microstructurally by X-ray diffractometry (XRD; D8 Advance, Bruker AXS, Germany), scanning electron microscopy (SEM; S-3600N, Hitachi, Japan or Quanta 3D, FEI, The Netherlands), and energy-dispersive X-ray spectrometry (EDS; Xflash Detector 3001, Röntec GmbH, Germany). The mechanical characterization (hardness and toughness) was done by Vickers indentation tests (MV-1, Matsuzawa, Japan) on the polished surface of selected SPS-ed samples.

Model SPS experiments were also conducted to investigate in detail the microstructural development of the B_4C composites. To this end, the B_4C powder with 15 vol.% $MoSi_2$ was SPS-ed at temperatures in the range 1150-1500 °C. Modified SPS cycles (100 °C/min heating, 50 MPa pressure, dynamic-vacuum atmosphere) without soaking time were used, in which just immediately after reaching the desired target SPS temperature the electrical power of the SPS furnace was intentionally shut off and the pressure was deliberately released. The resulting B_4C composites were ground, and were all characterized microstructurally by XRD and some selectively by SEM.

3. Results and Discussion

Figures 1-4 show representative SEM images of all the materials fabricated, and Table 1 gives the degrees of densification (qualitative information) inferred from the extensive microstructural observations. It can be seen that the degree of densification increases with both the target SPS temperature and the $MoSi_2$ proportion. The former was expected (diffusion is a thermally-activated process obeying an Arrhenius-type law [31]), while the latter proves that $MoSi_2$ is a suitable SPS additive for B_4C. Note that the differences of densification are attributable to effects of temperature and composition, and not to electrical effects because during SPS (*i*) the voltages applied were very low (~ 6 V) and nearly the same in all cases (difference of less than ~0.22 V), which would exclude field effects, and (*ii*) the amperages applied were also, for a given temperature, nearly the same regardless of the $MoSi_2$ content used as sintering additive (difference of less than ~1.4%), which would rule out current effects. Importantly, it can be seen that the monolithic ceramics are all to a greater or lesser extent porous, although the one SPS-ed at 1850 °C is near fully-dense. On the contrary, all the composites eventually densified completely, in particular, at target SPS temperatures of 1850 (5 vol.% $MoSi_2$), 1800 (10 vol.% $MoSi_2$), and 1750 °C (15 vol.% $MoSi_2$). In addition, at ~50 °C below these temperatures they reached near full-densification. It can also be seen in Figs. 2-4 that the composites contain Mo/Si-rich second phases over their entire microstructure. This was further confirmed by EDS compositional maps, an example of which is shown in Fig. 5. There are however pockets of Mo/Si-rich second phases, which indicates that their distribution is not completely uniform. This is attributable to the difference between the particle sizes of the B_4C (~0.3-0.6 µm) and $MoSi_2$ (~3.5-5 µm) powders, and therefore future processing efforts are needed to gain in microstructural homogeneity (for example introducing a step of ball-

milling/co-ball milling, using colloidal processing, or simply utilizing starting powders with more similar granulometric features).

Figure 6 shows the SPS densification curves as a function of temperature for the B_4C powder with different $MoSi_2$ contents (i.e., 0, 5, 10, and 15 vol.%). Overall, these curves have the three-stretch shape observed for other refractory carbides and borides [32-39]. Specifically, there are two stretches during the non-isothermal heating, the first of moderate densification attributable to mechanical powder compaction and the second of accelerated densification attributable to diffusion inducing mass transport. Lastly, there is a third stretch of gradual densification during the isothermal heating. Table 2 lists the ultimate densifications reached, which are not necessarily 100%.[IV] The SPS densification curves thus confirm that B_4C sinterability increases with the $MoSi_2$ proportion because the densification kinetics speeds up. Thus for example, the intermediate sintering regime [40][V] was reached at ever lower temperatures during the non-isothermal heating, in particular at ~1770 (0 vol.% $MoSi_2$), 1685 (5 vol.% $MoSi_2$), 1600 (10 vol.% $MoSi_2$), and 1550 °C (15 vol.% $MoSi_2$). The final sintering regime[V] was also reached earlier with increasing $MoSi_2$ proportion, in particular after ~130 s at 1800 °C or 80 s at 1850 °C for 0 vol.% $MoSi_2$, after ~50 s at 1800 °C or 10 s at 1850 °C for 5 vol.% $MoSi_2$, at ~1790 °C for 10 vol.% $MoSi_2$, and at ~1700 °C for 15 vol.% $MoSi_2$.

The SPS densification curves are also a reflection of the $MoSi_2$ addition altering the sintering mechanism of B_4C. This is clearer however in the shrinkage rate curves, an example of which is shown in Fig. 7 for the B_4C powder without and with 15 vol.% $MoSi_2$. The curve of the

[IV] When this happens, prolonging the SPS cycle is of little or no effectiveness because densification tends towards a certain limiting value. This is more evident when the SPS densification curves are plotted as a function of time.

[V] The intermediate sintering regime is that during which the pore distribution transforms from open porosity to closed porosity, and is typically taken to begin at ~70% relative density. The final sintering regime is that during which the closed porosity is eliminated, and is normally taken to start at ~90% relative density.

former reflects a partial densification by solid-state sintering because the shrinkage rate first remains invariably low up to the sintering onset temperature (~1420 °C), and then increases gradually with temperature. But the curve of the latter exhibits a distinctive peak of accelerated shrinkage rate at ~1390 °C, and sintering started long before (at ~1300 °C). This peak is indicative of densification by liquid-phase sintering, and in particular is associated with the sudden formation of a liquid that spreads rapidly between grains, filling the pores. The rest of the curve follows the expected temperature dependence, with the shrinkage rate increasing gradually up to the temperature of most active sintering, and then decreasing [40].

Figure 8 compares, by way of example, representative SEM images of the microstructure of both the monolithic ceramic and the composite with 15 vol.% $MoSi_2$ SPS-ed at 1800 °C. It can be seen that while the former is porous and fine-grained, the latter is fully dense and also has a more complex triplex-particulate microstructure. According to EDS analyses shown in Fig. 9, the major phase is rich in B and C, whereas the other grains are rich in either Si and C or Mo and B. Clusters of these grains were also observed in the lower-magnification SEM observations, which is consistent with the earlier observations (Figs. 2-4).

Figure 10 shows the XRD patterns of all the materials fabricated. It can be seen that the monolithic ceramics contain only B_4C and some residual graphite (an impurity already present in the B_4C starting powder [19,41,42]). The composites, however, contain B_4C plus various additional compounds, none of which is $MoSi_2$. These are SiC (cubic polytype (β-SiC)) and MoB_2 (trigonal and hexagonal polymorphs (β-MoB_2 and α-MoB_2, respectively)). This then is consistent with the EDS analyses. Of the two MoB_2 polymorphs, β-MoB_2 predominates for SPS temperatures up to ~1750 °C, whereas α-MoB_2 does so thenceforward. Previous work has also shown that β-MoB_2 and α-MoB_2 are, respectively, low- and high-temperature polymorphs [43].

There is also some, but less, residual graphite in the composites fabricated with 5 vol.% $MoSi_2$, but not in those made with 10 and 15 vol.% $MoSi_2$. The present composites fabricated by SPS and their counterparts fabricated earlier by hot-pressing thus have the same phase composition, because the trigonal-Mo_2B_5 compound that has been reported for the latter [30] is actually β-MoB_2 [44,45].[VI]

Thus, the above results reveal that the whole of the $MoSi_2$ reacted with part of the B_4C during SPS. A possible global reaction path would be:

$$B_4C + 2MoSi_2 + 3C \rightarrow 4SiC + 2MoB_2 \qquad (1)$$

where the C reactant comes from the graphite impurities in the B_4C starting powders and/or is taken up during SPS (diffusion from the graphite tools and/or foils). This reaction has already been proposed for the hot-pressed B_4C composites [30].[VII] Another possible global reaction path would be:

$$2B_4C + 4MoSi_2 + 6CO(g) \rightarrow 8SiC + 4MoB_2 + 3O_2(g) \qquad (2)$$

where the CO(g) reactant would be generated in-situ during SPS because the graphite tools/foils are heated under low oxygen partial pressure (due to the dynamic vacuum during SPS). There were however two experimental observations in favour of the occurrence of Reaction (1). Firstly, the B_4C-$MoSi_2$ powder mixtures did not emit more gas (attributable to O_2 release) than the B_4C powder. By way of example, Fig. 11 compares the vacuum levels registered for the B_4C powder without and with 15 vol.% $MoSi_2$ SPS-ed at 1700 °C, illustrating this observation. This is indeed

[VI] It is now well established that what was formerly described as trigonal-Mo_2B_5 is actually trigonal-Mo_2B_4 (i.e., β-MoB_2) because crystallographic studies have demonstrated that Mo_2B_5 is actually a non-stoichiometric compound without the centring boron atoms in the puckered sheets of condensed cyclohexane-like boron chairs.

[VII] An analogous reaction (i.e., $5B_4C + 8MoSi_2 + 11C \rightarrow 16SiC + 4Mo_2B_5$) was also formulated to explain the (now known to be wrong) formation of Mo_2B_5 (and concurrently of more SiC as well), but of course this reaction can never take place because Mo_2B_5 is actually β-MoB_2.

the result expected from Reaction (1), whereas Reaction (2) predicts the opposite result. And secondly, C is necessarily one of the reactants because the graphite impurities in the B_4C starting powders were consumed only when there was $MoSi_2$. This is the case of Reaction (1), but not of Reaction (2). Also note that Reaction (1) has been proved to be thermodynamically enabled in the range of SPS temperatures used [30]. Having identified that the overall reaction path is Reaction (1), one can then calculate that the composites fabricated with 5, 10, and 15 vol.% $MoSi_2$ have a B_4C-MoB_2-SiC composition in wt.% of 85.9-8.4-5.7, 73.7-15.6-10.7, and 63.2-21.9-14.9, respectively.

The conclusion is that $MoSi_2$ acted as a reactive sintering additive, not as a permanent sintering additive. $MoSi_2$ is not the first transient sintering additive used to densify B_4C with in-situ formation of refractory carbides and borides [18,19], but it can offer certain advantages over the others. In particular, it will also notably increase the oxidation resistance of B_4C at high temperatures, which otherwise would undergo non-protective passive or active oxidations due to the formation of a liquid B_2O_3 scale or gaseous B_2O_3 [46]. Thus, the numerous oxidation studies carried out on boride-based UHTCs indicate that the SiC grains in the microstructure of the present composites will oxidize to SiO_2, which will react with the B_2O_3 resulting from the oxidation of the B_4C grains, thus developing protective borosilicate-glass scales [47-49]. This might allow the use of these composites at high temperatures in oxidizing atmospheres, which are conditions that the monolithic B_4C ceramics normally do not withstand. Indeed, a recent study [50] has confirmed experimentally that the B_4C-ZrB_2-SiC triplex-particulate composites have greater oxidation resistance than the monolithic B_4C ceramics.

To identify the sintering mechanism of these B_4C-MoB_2-SiC composites, additional model SPS experiments were conducted on the B_4C powder with 15 vol.% $MoSi_2$. They

consisted in interrupting deliberately the SPS cycle at preselected temperatures in the range 1150-1500 °C by shutting off the electrical power of the furnace and releasing the pressure. Owing to the ultra-fast cooling to room-temperature of the SPS furnace, these samples provide "frozen snapshots" of the microstructural development of the composites. Figure 12 shows the XRD patterns of some selected composites resulting from these interrupted SPS experiments. It can be seen that the composite SPS-ed at 1150 °C contains B_4C, H_3BO_3 (typical impurity in this and in other B_4C starting powders [19,41,42,51,52]),[VIII] C (impurity in the B_4C starting powder 19,41,42]), and $MoSi_2$, plus β-MoB_2, SiC, and Si in minor amounts. The reaction of in-situ formation of refractory carbides and borides thus began slightly below 1150 °C, with Si being another reaction product. The composites SPS-ed between 1150 and 1350 °C had the same phase inventory, but with less H_3BO_3 and $MoSi_2$ and more β-MoB_2, SiC, and Si as the SPS temperature increased. This was also the trend observed for the composites SPS-ed at 1400 and 1450 °C, but with the difference that they no longer contain crystalline H_3BO_3, but nevertheless some α-MoB_2. Lastly, the composite SPS-ed at 1500 °C is formed by B_4C, C, SiC, β-MoB_2, α-MoB_2, and Si, but not $MoSi_2$. Consequently, B_4C finished consuming all the $MoSi_2$ at a temperature between 1450 and 1500 °C. According to their XRD patterns (Figs. 10C-D), the B_4C composites SPS-ed at higher temperatures (i.e., ≥1700 °C) have only B_4C, SiC, and MoB_2, reflecting that Si and C eventually consume each other at a temperature between 1500 and 1700 °C. Concomitantly, the composites become richer in α-MoB_2 at the expense of β-MoB_2. Figure 13 shows representative SEM images of the composites resulting from the model SPS experiments interrupted at 1250 and 1400 °C. As expected, the two composites are still extremely porous. The relevant microstructural observation is that, whereas the former exhibits only particles in a very

[VIII] H_3BO_3 will dehydrate into B_2O_3 during heating ($2H_3BO_3 \rightarrow B_2O_3+3H_2O(g)$), and will re-hydrate again during cooling down to room temperature.

early adhesion state (incipient sinter bond), the latter already exhibits dense regions with a molten phase embedding the particles. According to the EDS analyses (not shown), that phase is Si.

It is then clear that the formation of refractory carbides (i.e., SiC) and borides (i.e., MoB_2) in-situ during SPS actually came accompanied by the formation of Si as an intermediate component, and consequently that Reaction (1) really occurred in the following two sub-steps:

$$B_4C + 2MoSi_2 \rightarrow SiC + 2MoB_2 + 3Si \quad (3.1)$$

$$3Si(l) + 3C \rightarrow 3SiC \quad (3.2)$$

Thus, the $MoSi_2$ sintering additive reacts with B_4C to form MoB_2 (mostly β-MoB_2) and SiC, plus free Si (Reaction (3.1)). This first reaction starts slightly below 1150 °C, and is complete at ~1450-1500 °C (Fig. 12). Importantly, this reaction does not itself play a role in the densification because the SPS densification curves (Figs. 6B-D) and the shrinkage rate curves (Fig. 7) show no signs of enhanced densification below ~1300 °C. Eventually during the heating ramp the SPS temperature reaches ~1410 °C or more, and therefore free Si melts. This molten Si quickly spreads and wets efficiently the neighbouring particles (Figs. 13B-C), thus increasing the densification by both pore filling and particle rearrangement. This explains the accelerated shrinkage rate observed in the B_4C-$MoSi_2$ powder mixtures at ~1390 °C (Fig. 7).[IX] Nonetheless, as seen in both the SPS densification curves (Figs. 6B-D) and the SEM observations (Figs. 13B-C), the amount of molten Si formed is insufficient to reach complete densification only by pore filling and particle rearrangement. As the SPS temperature increases further during the heating ramp, molten Si reacts with the C impurities of the B_4C starting powder producing more SiC (Reaction (3.2)). This second reaction occurs at a temperature between 1500 and 1700 °C (Figs.

[IX] Note that the actual temperature within the graphite die is slightly greater than that measured by the optical pyrometer focused on the interior of the upper graphite punch.

10 and 12). Si is therefore a transient component that does not jeopardize the refractoriness of these composites. Finally, once all the molten Si has been consumed forming SiC, during the rest of the SPS cycle the composites continue to densify gradually by conventional solid-state sintering at a lower rate until their full densification. Concomitantly, β-MoB_2 progressively transforms polymorphically to α-MoB_2. Consequently, despite its high melting point of ~1930 °C, $MoSi_2$ then promotes the lower-temperature densification of B_4C by transient liquid-phase sintering.

Table 2 also lists the hardness of all the materials fabricated. It can be seen that it always increases to or above 25 GPa with increasing target SPS temperature, as expected for B_4C-based materials. Importantly, for the same given target SPS temperature, the composites are always harder than their reference monolithic ceramic. In addition, the higher the $MoSi_2$ content used as sintering additive, the greater the difference in hardness between the composite and the monolithic ceramic. To put these differences in perspective, note for example that the monolithic ceramic SPS-ed at 1750 °C is very soft (~14 GPa hardness), whereas the corresponding composite fabricated with 15 vol.% $MoSi_2$ is super-hard (~30 GPa hardness). The hardest of the monolithic ceramics (i.e., the one SPS-ed at 1850 °C) also reached an ultra-high hardness of ~25 GPa, but this is far less than expected for super-hard B_4C (i.e., ~35 GPa). Besides the residual graphite that softens them, this essentially reflects that the hardness of monolithic B_4C ceramics depends largely on their degree of densification, decreasing exponentially with a rate constant of ~7 as the residual porosity increases [53]. Indeed, near fully-dense monolithic B_4C ceramics have a hardness in the range ~25-29 GPa [54,55]. The same is the case for the composites, whose hardness also increases gradually up to ~30 GPa as their residual porosity decreases. It is a little surprising, however, that the hardness of the fully-dense composites is independent of the $MoSi_2$

content used as sintering additive (in the range 5-15 vol.%). This is attributable to the differences in their phase compositions. Firstly, the fully-dense composite fabricated with 5 vol.% $MoSi_2$ contains some residual graphite (Fig. 10B; SPS-ed at 1850 °C), and is therefore softer. And secondly, the fully-dense composites fabricated with 5, 10, and 15 vol.% $MoSi_2$ contain, respectively, α-MoB_2 but no β-MoB_2 (Fig. 10B; SPS-ed at 1850 °C), much α-MoB_2 and a little β-MoB_2 (Fig. 10C; SPS-ed at 1800 °C), and a little α-MoB_2 and much β-MoB_2 (Fig. 10D; SPS-ed at 1750 °C), and α-MoB_2 is much softer than β-MoB_2 (~13 vs 19 GPa at 9.8 N) [43]. The net result is that increasing the $MoSi_2$ content in the powder mixtures enhances B_4C sinterability without any deterioration in the hardness of the resulting composites – at least up to 15 vol.% $MoSi_2$. Finally, one also observes in Table 2 that, for the same degree of densification, the monolithic ceramics are harder than the composites, which is because B_4C is harder than SiC, α-MoB_2, and β-MoB_2.

There are more triplex-particulate composites based on B_4C that are ultra-hard/super-hard, namely (relative composition in volume fractions): $1B_4C$-$1TiB_2$-1SiC (~33 GPa) [56], $15B_4C$-$70TiB_2$-15SiC (~30.9 GPa) [56], $1B_4C$-$1ZrB_2$-1SiC (~28.9 GPa) [57], $90B_4C$-$8ZrB_2$-2SiC (~29 GPa) [50], $80B_4C$-$16ZrB_2$-4SiC (~30 GPa) [50], and $70B_4C$-$24ZrB_2$-6SiC (~27 GPa) [50]. Interestingly, they were all fabricated by conventional solid-state sintering using hot-pressing [50,56,57], not by transient liquid-phase assisted SPS as done here. This suggests that triplex-particulate composites based on B_4C, SiC and early-transition metal diborides are a novel family of potentially ultra-hard/super-hard materials, as could also be the case for other possible combinations of three or more carbides and borides.

Table 2 also gives the fracture toughness of the fully-dense materials. Vickers testing is not applicable to measure the fracture toughness of porous brittle materials, and therefore the

reference toughness will be the ~1.9-2.3 MPa·$m^{1/2}$ measured earlier by single edge V-notched beam tests for fine-grained fully-dense monolithic B_4C ceramics [53]. It can then be seen that the composites are increasingly tougher than the monolithic ceramic with increasing $MoSi_2$ content used as sintering additive. This attribute thus adds to the enhanced sinterability without hardness penalization. As with other B_4C composites [58], this greater fracture toughness is because the increasing residual stresses [59,60][X] induced by the thermoelastic mismatches between the B_4C, MoB_2, and SiC grains result in microstructures with increasingly weak interfaces that favour crack deflection and bridging.

Let us now discuss some final considerations that arise from the present study that are of interest for the ceramics community in general, and for that of hard materials in particular. Firstly, while dense monolithic B_4C ceramics are very challenging to fabricate, on the contrary, it is relatively easy to fabricate, maybe even by conventional pressureless sintering, dense multi-particulate composites based on B_4C plus SiC and one or various refractory diborides (i.e., MeB_2, Me = Ti, Zr, Hf, V, Nb, Ta, Cr, Mo, W, and Re) from powder mixtures of B_4C with the corresponding early-transition metal disilicide(s) (i.e., $MeSi_2$). These composites are expected to possess a unique generic combination of ultra-high/super-high hardness, enhanced toughness, and superior oxidation resistance, not to mention other properties such as strength, wear resistance, etc., and therefore to hold great promise for structural applications. This could also be the case for the alternative multi-particulate composites fabricated (foreseeably at even lower temperatures) from powder mixtures of B_4C with aluminide(s) (i.e., $ZrAl_3$, $TiAl_3$, $TaAl_3$, etc.) instead of silicide(s). Future research needs to be encouraged that is targeted at investigating the relationships between the processing, microstructure, and properties of such families of B_4C

[X] Thermoelastic residual stress exhibits a parabolic functional dependence on the volume fraction of second phases.

composites. Secondly, the fact that the molten phase formed eventually reacts with C presents a unique opportunity for further toughening these B_4C composites via innovative microstructural designs. Specifically, in principle it seems potentially possible to fabricate B_4C composites reinforced in-situ with an ample variety of hard carbide phases of high aspect ratio, and therefore superior toughening effect, simply by introducing intentionally in the starting powder mixtures carbon nanotubes, graphene nanoplatelets, reduced graphene oxide nanosheets, carbon fibres, or other high aspect ratio carbonaceous phases as the carbon source for Reaction (3.2). There is thus a requirement for the stimulation of new processing efforts to make these appealing B_4C composites a reality. And thirdly, there remain important scientific aspects to be clarified. For example, it is unclear whether, in the absence of a solid carbon source in the powder mixtures, the CO(g) generated in the graphite furnaces would react with the molten phase to form more refractory carbide if this reaction were thermodynamically possible. If this reaction does not take place, it would then be important to determine whether the molten phase (L) remains in the microstructure as a residual secondary phase or, on the contrary, disappears either by entering in substitutional solid solution within the B_4C host to form $B_4(C,L)$ or by reacting with B_4C to form a C-deficient B_4C plus a refractory carbide. Indeed, new studies aimed at answering these questions are expected. In sum, the multi-particulate composites based on B_4C plus refractory borides and carbides fabricated in-situ at fairly smooth sintering conditions constitute a fertile ground for future research framed within one of the eight grant challenges (i.e., that of ceramics for extreme environments) with societal import identified recently by the ceramics community [61].

4. Summary

Super-hard monolithic B_4C ceramics are very appealing for many engineering applications, but brittle and difficult to densify. To palliate these two weaknesses, here $MoSi_2$ additives were used to fabricate B_4C multi-particulate composites with superior toughness (~3-4 $MPa \cdot m^{1/2}$) and super-high hardness (~30 GPa) by SPS at lower temperatures. It was demonstrated that increasing $MoSi_2$ addition (in the range 5-15 vol.%) benefits B_4C sinterability and toughness, without penalizing its hardness. It was also demonstrated that the B_4C-$MoSi_2$ powder mixtures lead to B_4C-MoB_2-SiC triplex-particulate composites with fine-grained microstructures, and that $MoSi_2$ acts a reactive sintering additive that promotes the lower-temperature densification by transient liquid-phase sintering. Finally, research opportunities were presented for the future microstructural design of novel structural ceramic composites based on B_4C plus refractory borides and carbides.

Acknowledgements. This work was supported by the Ministerio de Economía y Competitividad (Government of Spain) and FEDER Funds under Grant nº MAT2016-76638-R. Financial support from the Junta de Extremadura under Grant nº GR15078, also co-financed with FEDER Funds, is gratefully acknowledged as well. Thanks are also due to Dr Xiaoxian Zang (on leave from Nanjing Tech University) for the technical assistance provided.

References

1. R. Riedel, Handbook of Ceramic Hard Materials, Weinheim: Wiley- VCH; 2000.
2. R.H. Wentorf, R.C. Devries, F.P. Bundy, Sintered superhard materials, Science 208 [4446] (1980) 873–880.
3. C.-M. Sung, M. Sung, Carbon nitride and other speculative superhard materials, Mat. Chem. Phys 43 [1] (1996) l–18.
4. S. Vepřek, The search for novel, superhard materials, J. Vac. Sci. Tech. A 17 [5] (1999) 2401–2420.
5. F. Thevenot, Boron carbide - a comprehensive review, J. Eur. Ceram. Soc. 6 [4] (1990) 205–225.
6. V. Domnich, S. Reynaud, R.A. Haber, M. Chhowalla, Boron carbide: structure, properties, and stability under stress, J. Am. Ceram. Soc. 94 [11] (2011) 3605–3628.
7. D. Rafaja, V. Klemm, M. Motylenko, M. R. Schwarz, T. Barsukova, E. Kroke, D. Frost, L. Dubrovinsky, N. Dubrovinskaia, Synthesis, microstructure, and hardness of bulk ultrahard BN nanocomposites, J. Mater. Res. 23 [4] (2008) 981–993.
8. D.M. Teter, R.J. Hemley, Low-compressibility carbon nitrides, Science 271 [5245] (1996) 53–55.
9. V.L. Solozhenko, D. Andrault, G. Fiquet, M. Mezouar, D.C. Rubie, Synthesis of superhard cubic BC_2N, Appl. Phys. Lett.78 [10] (2001) 1385–1387.
10. G. Akopov, M.T. Yeung, R.B. Kaner, Rediscovering the crystal chemistry of borides, Adv. Mater. 29 [21] (2017) 160450.
11. J.B. Levine, S.H. Tolbert, R.B. Kaner, Advancements in the search for superhard ultra-incompressible metal borides, Adv. Funct. Mater. 19 [22] (2009) 3519–3533.

12. D. He, Y. Zhao, L. Daemen, J. Qian, T.D. Shen, Boron suboxide: as hard as cubic boron nitride, Appl. Phys. Lett.81 [4] (2002) 643–645.
13. O.O. Kurakevych, V.L. Solozhenko, Experimental study and critical review of structural, thermodynamic and mechanical properties of superhard refractory boron suboxide B_6O, J. Superhard Mater. 33 [6] (2011) 421–428.
14. A.K. Suri, C. Subramanian, J.K. Sonber, T.S.R.-Ch. Murthy, Synthesis and consolidation of boron carbide: a review, Int. Mater. Rev. 55 [1] (2010) 4–40.
15. S.L. Dole, S. Prochazka, R.H. Doremus, Microstructural coarsening during sintering of boron carbide, J. Am. Ceram. Soc. 72 [6] (1989) 958–966.
16. S.L. Dole, S. Prochazka, Densification and microstructure development in boron carbide, Ceram. Eng. Sci. Proc. 6 [7–8] (1985) 1151–1160.
17. H. Lee, R.F. Speyer, Pressureless sintering of boron carbide, J. Am. Ceram. Soc. 86 [9] (2003) 1468–1473.
18. W. Ji, R.I. Todd, W. Wang, H. Wang, J. Zhang, Z. Fu, Transient liquid phase spark plasma sintering of B_4C-based ceramics using Ti-Al intermetallics as sintering aid, J. Eur. Ceram. Soc. 36 [10] (2016) 2419–2426.
19. A.L. Ortiz, V.M. Candelario, R. Moreno, F. Guiberteau, Near-net shape manufacture of B_4C–Co and ZrC–Co composites by slip casting and pressureless sintering, J. Eur. Ceram. Soc. 37 [15] (2017) 4577–4584.
20. E. Wuchina, E. Opila, M. Opeka, W. Fahrenholtz, I. Talmy, UHTCs: ultra-high temperature ceramic materials for extreme environment applications, Interface 16 [4] (2007) 30–36.
21. D. Sciti, L. Silvestroni, A. Bellosi, High-density pressureless-sintered HfC-based composite, J. Am. Ceram. Soc. 89 [8] (2006) 2668–2670.

22. D. Sciti, S. Guicciardi,M Nygren, Densification and mechanical behavior of HfC and HfB_2 fabricated by spark plasma sintering, J. Am. Ceram. Soc. 91 [5] (2008) 1433–1440.
23. D. Sciti, S. Guicciardi, M Nygren, Spark plasma sintering and mechanical behaviour of ZrC-based composites, Scripta Mater 59 [6] (2008) 638–641.
24. L. Silvestroni, D. Sciti, J. Kling, S. Lauterbach, H.-J. Kleebe, Sintering mechanisms of zirconium and hafnium carbides doped with $MoSi_2$, J. Am. Ceram. Soc. 92 [7] (2009) 1574–1579.
25. L. Silvestroni, A. Bellosi, C. Melandri, D. Sciti, J.X. Liu, G. J. Zhang, Microstructure and properties of HfC and TaC-based ceramics obtained by ultrafine powder, J. Eur. Ceram. Soc. 31 [4] (2011) 619–627.
26. B. Núñez-González, A.L. Ortiz, F. Guiberteau, N.P. Padture, Effect of $MoSi_2$ content on the lubricated sliding-wear resistance of ZrC–$MoSi_2$ composites, J. Eur. Ceram. Soc. 31 [5] (2011) 877–882.
27. L. Charpentier, M. Balat-Pichelin, D. Sciti, L. Silvestroni, High temperature oxidation of Zr- and Hf-carbides: influence of matrix and sintering additive, J. Eur. Ceram. Soc. 33 [15–16] (2013) 2867–2878.
28. L. Pienti, D. Sciti, L. Silvestroni, A. Cecere, R. Savino, Ablation tests on HfC- and TaC-based ceramics for aeropropulsive applications, J. Eur. Ceram. Soc. 35 [5] (2015) 1401–1411.
29. E. Sánchez-González, O. Borrero-López, F. Guiberteau, A.L. Ortiz, Microstructural effects on the sliding-wear resistance of ZrC–$MoSi_2$ triboceramics fabricated by spark-plasma sintering, J. Eur. Ceram. Soc. 36 [13] (2016) 3091–3097.

30. S. Kumar, K. Sairam,J.K. Sonber, T.S.R.Ch. Murthy, V. Reddy, G.V.S. Nageswara Rao, T. Srinivasa Rao, Hot-pressing of $MoSi_2$ reinforced B_4C composites, Ceram. Inter. 40 [10 Part B] (2014) 16099–16105.

31. D.R. Poirier, G.H. Geiger, Transport phenomena in materials processing. Pennsylvania, USA: The Minerals, Metals & Materials Society; 1998.

32. V. Zamora, A.L. Ortiz, F. Guiberteau, M. Nygren, Crystal-size dependence of the spark-plasma-sintering kinetics of ZrB_2 ultra-high-temperature ceramics, J. Eur. Ceram. Soc. 32 [2] (2012) 271–276.

33. B. Núñez-González, A.L. Ortiz, F. Guiberteau, M. Nygren, Improvement of the spark-plasma-sintering kinetics of ZrC by high-energy ball-milling, J. Am. Ceram. Soc. 95 [2] (2012) 453–456.

34. V. Zamora, A.L. Ortiz, F. Guiberteau, M. Nygren, Spark-plasma sintering of ZrB_2 ultra-high-temperature ceramics at lower temperature via nanoscale crystal refinement, J. Eur. Ceram. Soc. 32 [10] (2012) 2529–2536.

35. V. Zamora, A.L. Ortiz, F. Guiberteau, M. Nygren, On the enhancement of the spark-plasma sintering kinetics of ZrB_2–SiC powder mixtures subjected to high-energy co-ball-milling, Ceram. Int. 39 [4] (2013) 4191–4204.

36. B. Núñez-González, A.L. Ortiz, F. Guiberteau, M. Nygren, Spark-plasma-sintering kinetics of ZrC–SiC powder mixtures subjected to high-energy co-ball-milling, Ceram. Int. 39 [8] (2013) 9691–9697.

37. A. Motealleh, A.L. Ortiz, O. Borrero-López, F. Guiberteau, Effect of hexagonal-BN additions on the sliding-wear resistance of fine-grained α-SiC densified with $Y_3Al_5O_{12}$ liquid phase by spark-plasma sintering, J. Eur. Ceram. Soc. 34 [3] (2014) 565–574.

38. V. Zamora, M. Nygren, F. Guiberteau, A.L. Ortiz, Effect of graphite addition on the spark-plasma sinterability of ZrB_2 and ZrB_2–SiC ultra-high-temperature ceramics, Ceram. Int. 40 [7 Part B] (2014) 11457–11464.

39. V.M. Candelario, R. Moreno, Z. Shen, F. Guiberteau, A.L. Ortiz, Liquid-phase assisted spark-plasma sintering of SiC nanoceramics and their nanocomposites with carbon nanotubes, J. Eur. Ceram. Soc. 37 [5] (2017) 1929–1936.

40. R.M. German, Sintering theory and practice. Wiley: New York; 1996.

41. F. Rodríguez-Rojas, R. Moreno, F. Guiberteau, A.L. Ortiz, Aqueous colloidal processing of near-net shape B_4C–Ni cermet compacts, J. Eur. Ceram. Soc. 36 [8] (2016) 1915–1921.

42. A.L. Ortiz, F. Sánchez-Bajo, V.M. Candelario, F. Guiberteau, Comminution of B_4C powders with a high-energy mill operated in air in dry or wet conditions and its effect on their spark-plasma sinterability, J. Eur. Ceram. Soc. 37 [13] (2017) 3873–3884.

43. Q. Tao, X. Zhao, Y. Chen, J. Li, Q. Li, Y. Ma, J. Li, T. Cui, P. Zhu, X. Wang, Enhanced Vickers hardness by quasi-3D boron network in MoB_2, RCS Adv. 3 [40] (2013) 18317–18322.

44. S. Okada, T. Atoda, I. Higashi, Y. Takahashi, Preparation of single crystals of MoB_2 by the aluminium-flux technique and some of their properties, J. Mat. Sci. 22 [8] (1987) 2993–2999.

45. M. Frotscher, W. Klein, J. Bauer, C. M. Fang, J. F. Halet, A. Senyshyn, C. Baehtz, B. Albert, M_2B_5 or M_2B_4? A reinvestigation of the Mo/B and W/B system, Z. Anorg. Allg. Chem. 633 [15] (2007) 2626–2630.

46. L.M. Litz, R.A. Mercuri, Oxidation of boron carbide by air, water, and air-water mixtures at elevated temperatures, J. Electrochem. Soc. 110 [8] (1963) 921–925.

47. M.M. Opeka, I.G. Talmy, J.A. Zaykoski, Oxidation-based materials selection for 2000 °C + hypersonic aerosurfaces: theoretical considerations and historical experience, J. Mater. Sci. 39 [19] (2004) 5887–5904.

48. W.G. Fahrenholtz, G.E. Hilmas, Oxidation of ultra-high temperature transition metal diboride ceramics, Intl. Mater. Rev. 57 [1] (2012) 61–72.

49. Lin Zhang, N.P. Padture, Inhomogeneous oxidation of ZrB_2-SiC ultra-high-temperature ceramic particulate composites and its mitigation, Acta Mater. 129 (2017) 138–148.

50. L. Hu, Z. Lu, R. He, H. Lei, Z. Qu, Y. Yang, D. Fang, Oxidation behavior of B_4C-(ZrB_2-SiC) ceramics at 1600 °C, Int. J. Refract. Met. Hard Mater 78 (2019) 282–287.

51. B.M. Moshtaghioun, A.L. Ortiz, D. Gómez-García, A. Domínguez-Rodríguez, Densification of B_4C nanopowder with nanograin retention by spark-plasma sintering, J. Eur. Ceram. Soc. 35 [6] (2015) 1991–1998.

52. B.M. Moshtaghioun, D. Gómez-García, A. Domínguez-Rodríguez, A.L. Ortiz, Enhancing the spark-plasma sinterability of B_4C nanopowders via room-temperature methylation induced purification, J. Eur. Ceram. Soc. 36 [11] (2016) 2843–2848.

53. B.M. Moshtaghioun, D. Gómez-García, A. Domínguez-Rodríguez, R.I. Todd, Grain size dependence of hardness and fracture toughness in pure near fully-dense boron carbide ceramics, J. Eur. Ceram. Soc. 36 [7] (2016) 1829–1834.

54. S. Eqtesadi, A. Motealleh, F.H. Perera, P. Miranda, A. Pajares, R. Wendelbo, F. Guiberteau, A.L. Ortiz, Fabricating geometrically-complex B_4C ceramic components by robocasting and pressureless spark plasma sintering, Scripta Mater. 145 (2018) 14–18.

55. A.L. Ortiz, V.M. Candelario, O. Borrero-López, F. Guiberteau, Sliding-wear resistance of pure near fully-dense B_4C under lubrication with water, diesel fuel, and paraffin oil, J. Eur. Ceram. Soc. 38 [4] (2018) 1158–1163.

56. E.W. Neuman, H.J. Brown-Shaklee, G.E. Hilmas, W.G. Fahrenholtz, Titanium diboride-silicon carbide-boron carbide ceramics with super-high hardness and strength, J. Am. Ceram. Soc. 101 [2] (2018) 497–501.

57. W.G. Fahrenholtz, E.W. Neuman, H.J. Brown-Shaklee, G.E. Hilmas, Superhard boride-carbide particulate composites, J. Am. Ceram. Soc. 93 [11] (2010) 3580–3583.

58. B.M. Moshtaghioun, A.L. Ortiz, D. Gómez-García, A. Domínguez-Rodríguez, Toughening of super-hard ultra-fine grained B_4C densified by spark-plasma sintering via SiC addition, J. Eur. Ceram. Soc. 33 [8] (2013) 1395–1401.

59. B.R. Lawn, N.P. Padture, L.M. Braun, S.J. Bennison, Model for toughness curves in two-phase ceramics: I, basic fracture mechanics, J. Am. Ceram. Soc. 76 [9] (1993) 2235–2240.

60. N.P. Padture, J.L. Runyan, S.J. Bennison, L.M. Braun, B.R. Lawn, Model for toughness curves in two-phase ceramics: II, microstructural variables, J. Am. Ceram. Soc. 76 [9] (1993) 2241–2247.

61. K.T. Faber, T. Asefa, M. Backhaus-Ricoult, R.K. Brow, J. Chan, S. Dillon, W.G. Fahrenholtz, M.W. Finnis, J.E. Garay, E. Garcia, Y. Gogotsi, S.M. Haile, J.W. Halloran, J. Hu, L. Huang, S. Jacobsen, E. Lara-Curzio, J. LeBeau, W.E. Lee, C.G. Levi, I. Levin, J.A. Lewis, D.M. Lipkin, K. Lu, J. Luo, J.P. Maria, L.W. Martin, S. Martin, G.L. Messing, A. Navrotsky, N.P. Padture, C.A. Randall, G.S. Rohrer, A. Rozenflanz, T. Schaedler, D. Schlom, A. Sehirlioglu, A. Stevensen, T. Tani, V. Tikare, S. Trolier-McKinstry, H. Wang, B. Yildiz, The role of

ceramic and glass science research in meeting societal challenges: report from an NSF-sponsored workshop, J. Am. Ceram. Soc. 100 [5] (2017) 1777–1803.

Figure Captions

Figure 1. Representative SEM micrographs of the fracture surface of the monolithic B_4C ceramics fabricated by SPS using target temperatures of (A) 1700, (B) 1750, (C) 1800, and (D) 1850 °C.

Figure 2. Representative SEM micrographs of the fracture surface of the B_4C composites fabricated by SPS using 5 vol.% $MoSi_2$ sintering additive and target temperatures of (A) 1800 and (B) 1850 °C.

Figure 3. Representative SEM micrographs of the fracture surface of the B_4C composites fabricated by SPS using 10 vol.% $MoSi_2$ sintering additive and target temperatures of (A) 1700, (B) 1750, and (C) 1800 °C.

Figure 4. Representative SEM micrographs of the fracture surface of the B_4C composites fabricated by SPS using 15 vol.% $MoSi_2$ sintering additive and target temperatures of (A) 1700, (B) 1750, and (C) 1800 °C.

Figure 5. (A) Representative SEM micrograph of the fracture surface of the B_4C composite fabricated by SPS using 15 vol.% $MoSi_2$ sintering additive and a target temperature of 1750 °C, and the corresponding elemental compositional maps of (B) Mo and (C) Si obtained by EDS.

Figure 6. Densification curves as a function of temperature for (A) the B_4C powder, and for the B_4C-$MoSi_2$ powder mixtures with (B) 5, (C) 10, and (D) 15 vol.% $MoSi_2$ logged during their SPS cycles with different target temperatures. The degrees of densification corresponding to the

onset of the intermediate (70%) and final (90%) stages of sintering are marked by dotted and dashed lines, respectively.

Figure 7. Shrinkage-rate curve as a function of temperature for the B_4C powder and for the B_4C-$MoSi_2$ powder mixture with 15 vol.% $MoSi_2$ logged during their SPS cycle with a target temperature of 1700 °C.

Figure 8. Representative SEM micrographs of the electrochemically-etched, polished surface of (A) the monolithic B_4C ceramic and (B) the B_4C composite with 15 vol.% $MoSi_2$ sintering additive fabricated by SPS using a target temperature of 1800 °C.

Figure 9. EDS spectra corresponding to the locations indicated by the numbers in Fig. 8B. Peak assignations are included. K and O come from the electrochemical etching with KOH solution. Si detected in 1, B and Mo detected in 2, and Si and C detected in 3 come from neighbouring grains because the effective interaction volume is larger than grain size.

Figure 10. XRD patterns of (A) the monolithic B_4C ceramics and of the B_4C composites with (B) 5, (C) 10, and (D) 15 vol.% $MoSi_2$ sintering additives fabricated by SPS using different target temperatures. Peak assignations are included.

Figure 11. Evolution of the vacuum level within the chamber of the SPS furnace as a function of temperature for the B_4C powder and for the B_4C-$MoSi_2$ powder mixture with 15 vol.% $MoSi_2$ logged during their SPS cycle with a target temperature of 1700 °C.

Figure 12. XRD patterns of the B_4C composites fabricated by SPS using 15 vol.% $MoSi_2$ sintering additive and cycles interrupted at 1150, 1400, 1450, and 1500 °C. Peak assignations are included. Logarithmic scales have been used to facilitate the observation of the weaker XRD peaks.

Figure 13. Representative SEM micrographs of the fracture surface of the B_4C composite with 15 vol.% $MoSi_2$ sintering additive fabricated by SPS using a cycle interrupted at (A) 1250 and (B) 1400 °C. (C) SEM micrograph at higher magnification of a region in (B), showing more detail.

Tables

Table 1. Fabrication conditions of all monolithic ceramics and ceramic composites, and their corresponding degrees of densification.

Type [&]	Target SPS temperature (°C) [#]			
	1700	**1750**	**1800**	**1850**
B_4C	✓ extremely porous	✓ very porous	✓ porous	✓ near-fully dense
B_4C-5vol.%$MoSi_2$	—	—	✓ near-fully dense	✓ fully dense
B_4C-10vol.%$MoSi_2$	✓ porous	✓ near-fully dense	✓ fully dense	—
B_4C-15vol.%$MoSi_2$	✓ near-fully dense	✓ fully dense	✓ fully dense	—

[&] Designations refer to the composition of the powder batches. [#] Other SPS conditions were: heating ramp of 100 °C/min and soaking time of 5 min at the target temperature. The lowest target SPS temperatures required to achieve near-full and full densification are in blue and red, respectively. The following five ranges of densification (d) have been defined: Full dense (d=100%), near-full dense (95≤d<100%), porous (90≤d<95%), very porous (80≤d< 90%), and extremely porous (d<80%).

Table 2. Fabrication conditions, degrees of densification achieved, and mechanical properties of the monolithic ceramics and ceramic composites.

Type [&]	Target SPS temperature (°C) [#]	Densification (%)	Hardness (GPa)	Fracture toughness (MPa·m $^{1/2}$)
B_4C	1700	78	13±1	—
	1750	82	14±1	—
	1800	93	19±1	—
	1850	95	25.0±0.7	—
B_4C-5vol.%$MoSi_2$	1800	96	19.8±0.8	—
	1850	100	29.5±0.9	3.1±0.2
B_4C-10vol.%$MoSi_2$	1700	93	15.0±0.5	—
	1750	96	20±1	—
	1800	100	30.1±0.9	3.7±0.3
B_4C-15vol.%$MoSi_2$	1700	97.5	23±1	—
	1750	100	30.1±0.7	4.1±0.3
	1800	100	30.1±0.6	4.1±0.3

[&] Designations refer to the composition of the powder batches. [#] Other SPS conditions were: heating ramp of 100 °C/min and soaking time of 5 min at the target temperature.

Figure

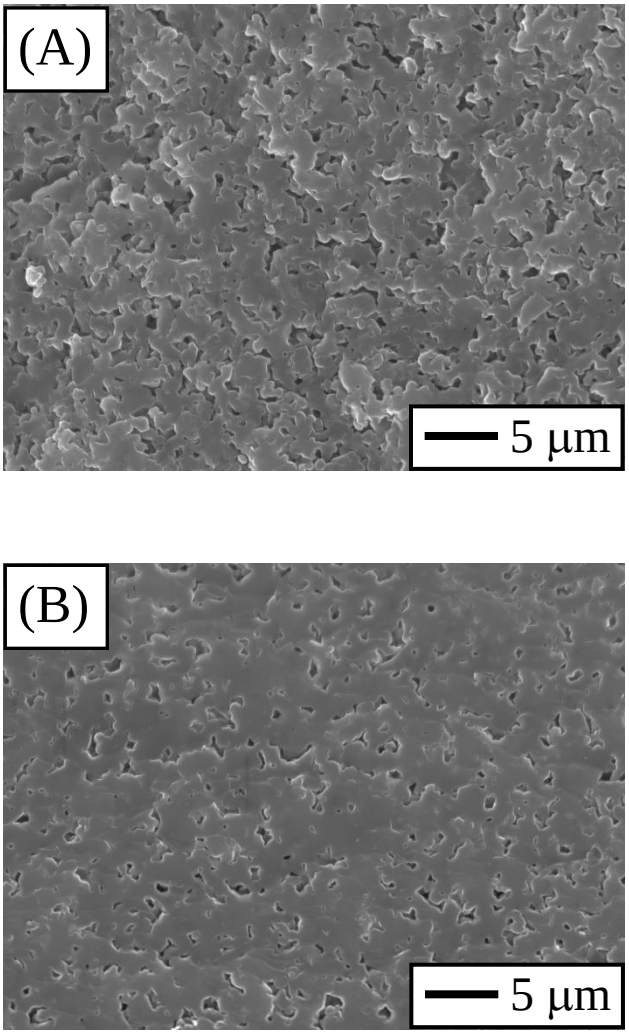

Ojalvo *et al.*
Figure 1

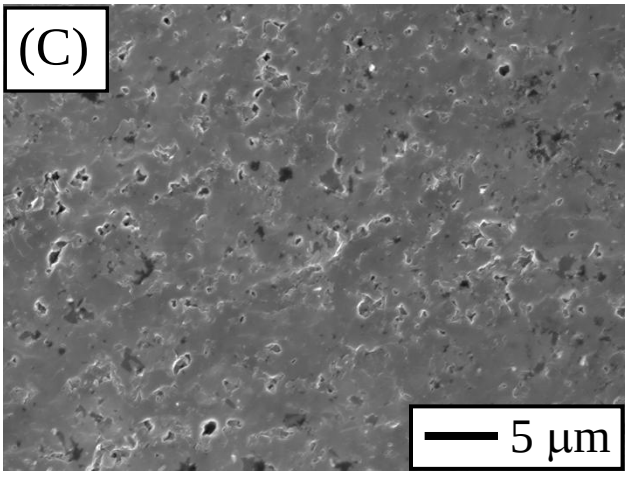

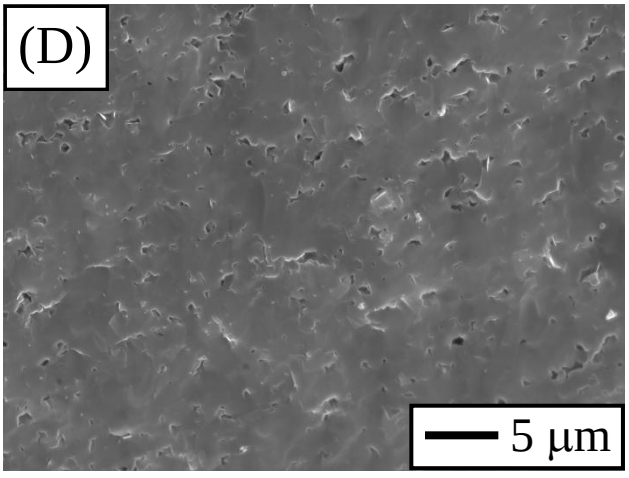

Ojalvo *et al.*
Figure 1

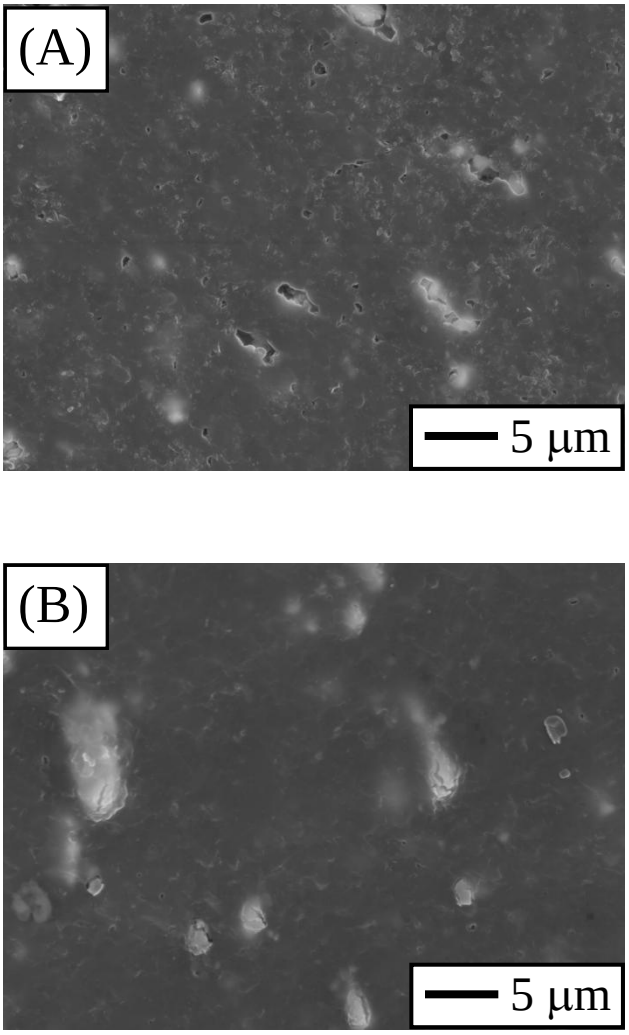

Ojalvo *et al.*
Figure 2

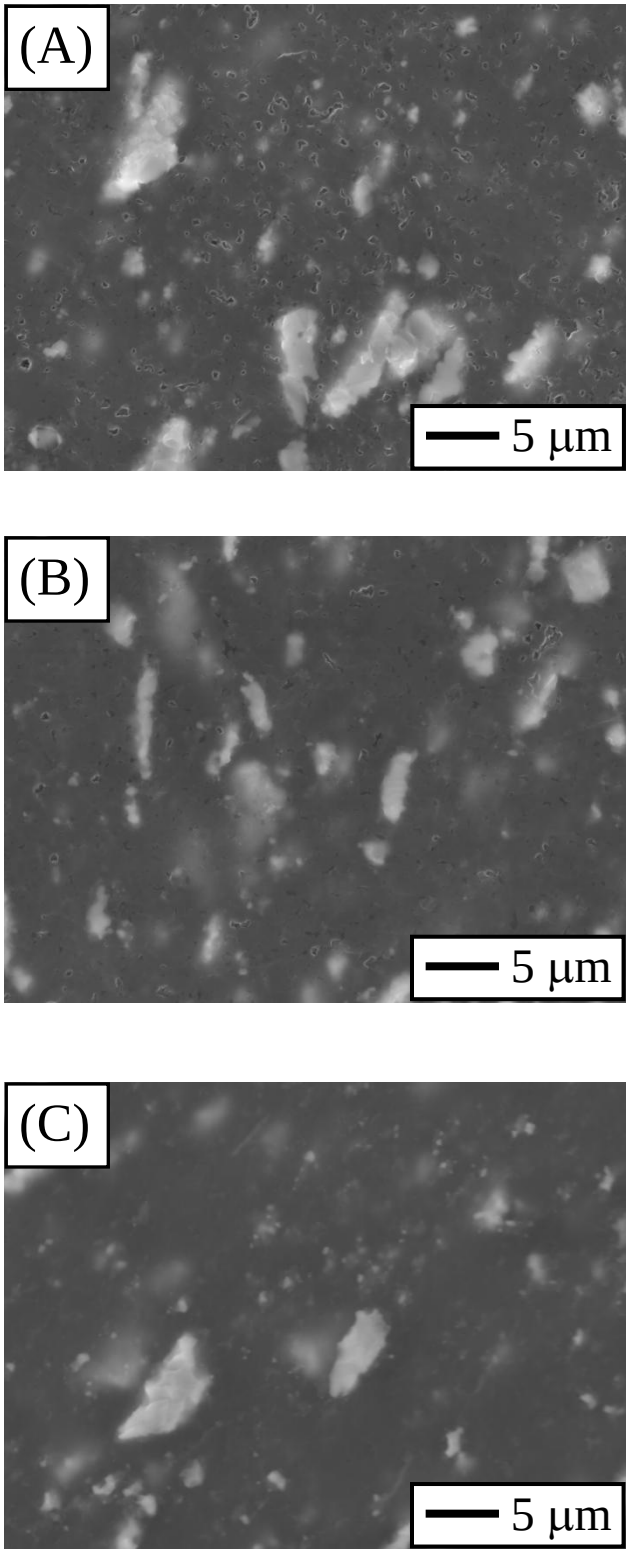

Ojalvo *et al.*
Figure 3

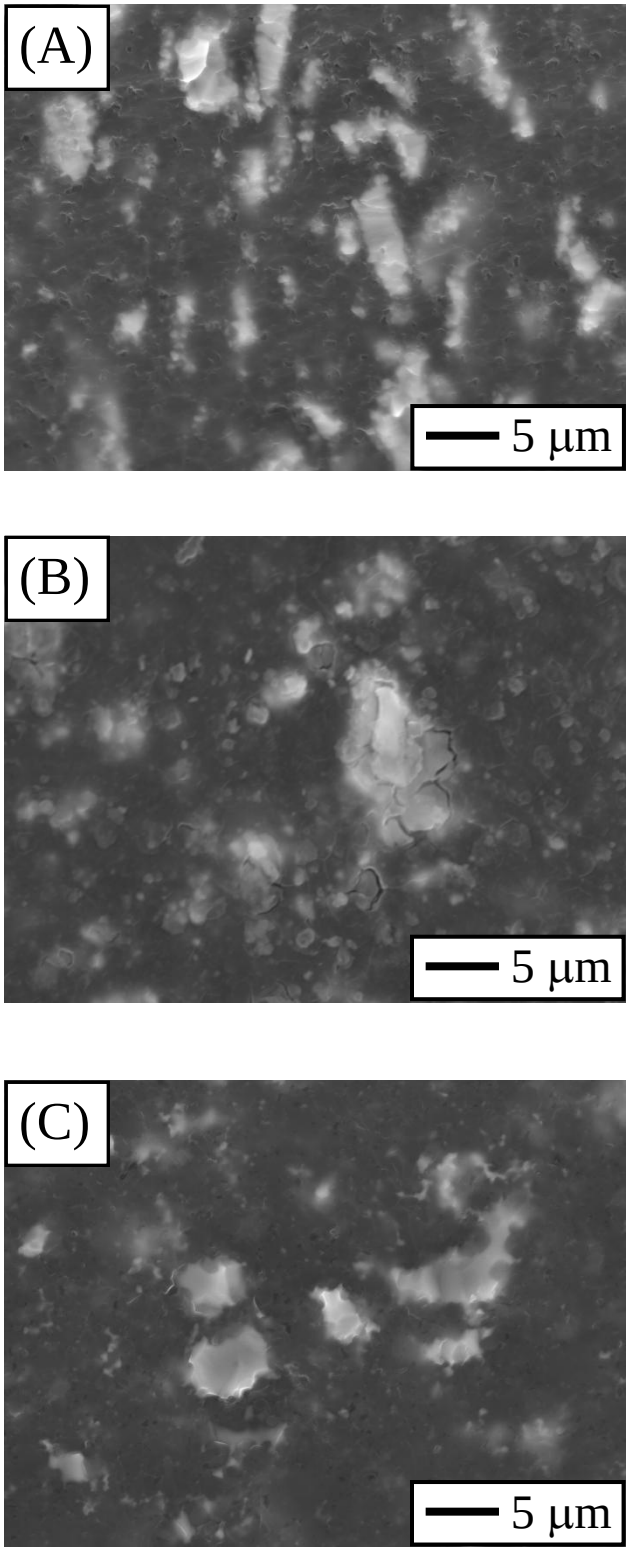

Ojalvo *et al.*
Figure 4

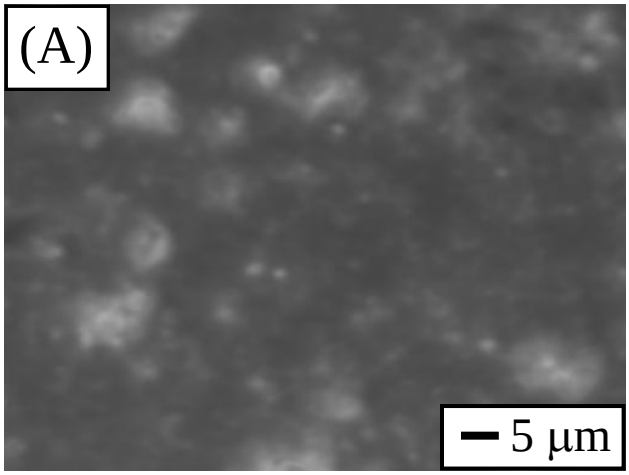

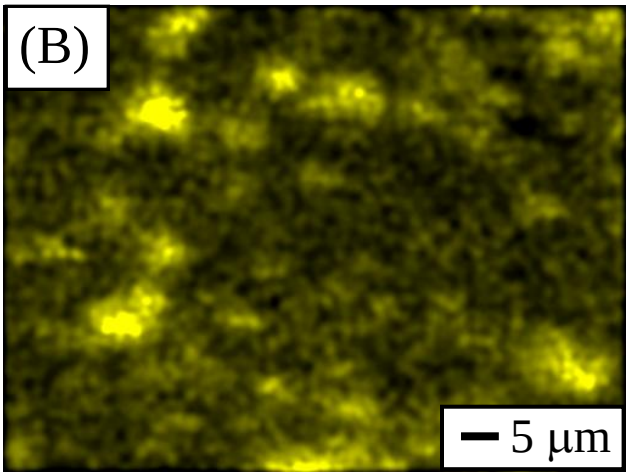

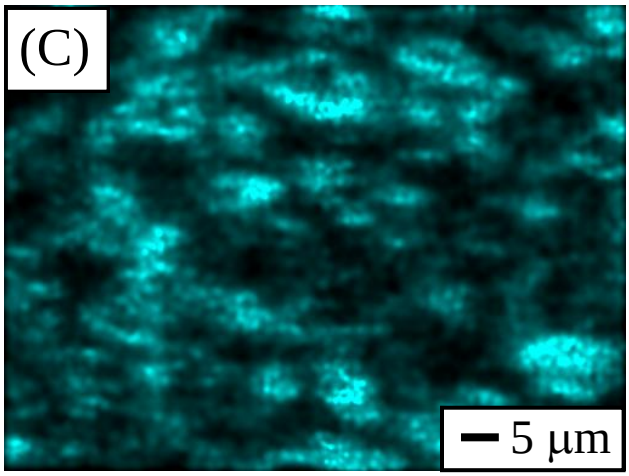

Ojalvo *et al.*
Figure 5

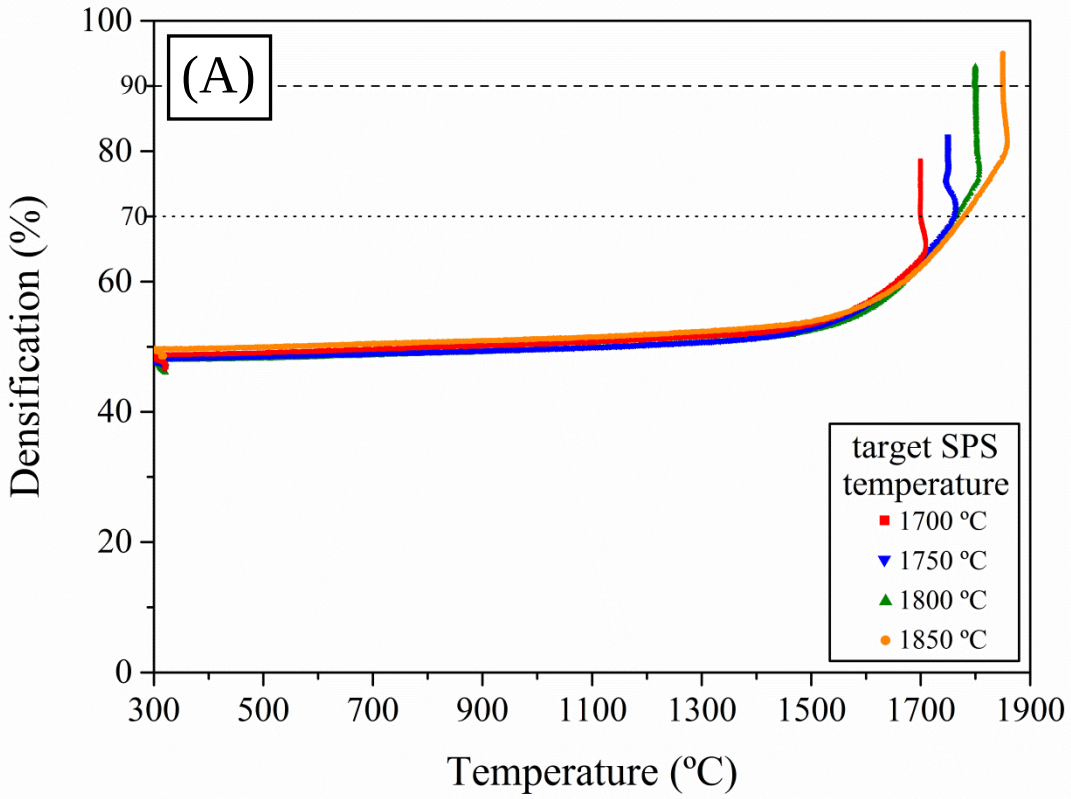

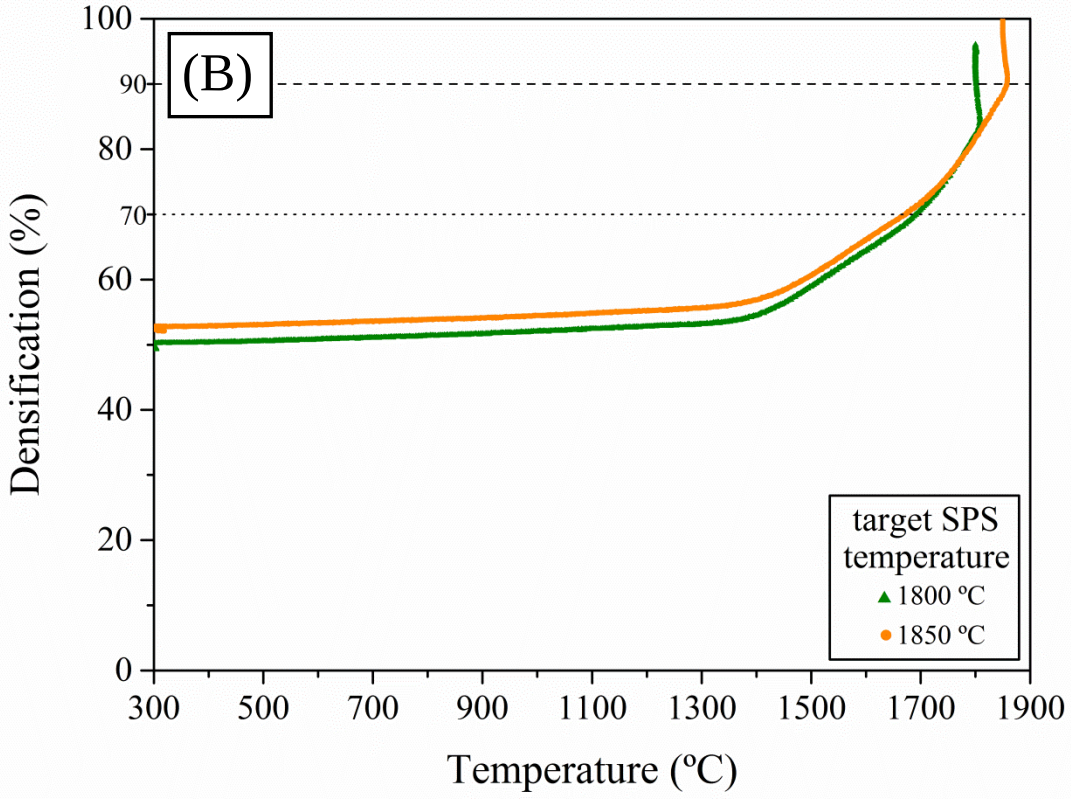

Ojalvo *et al.*
Figure 6

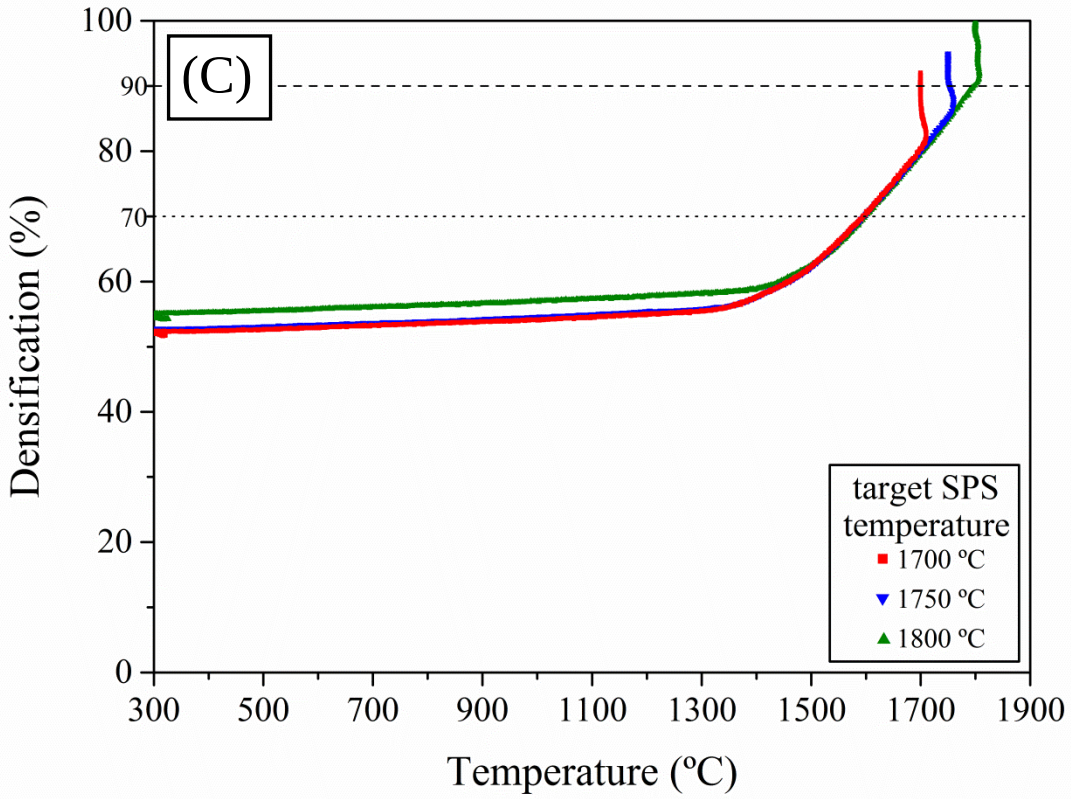

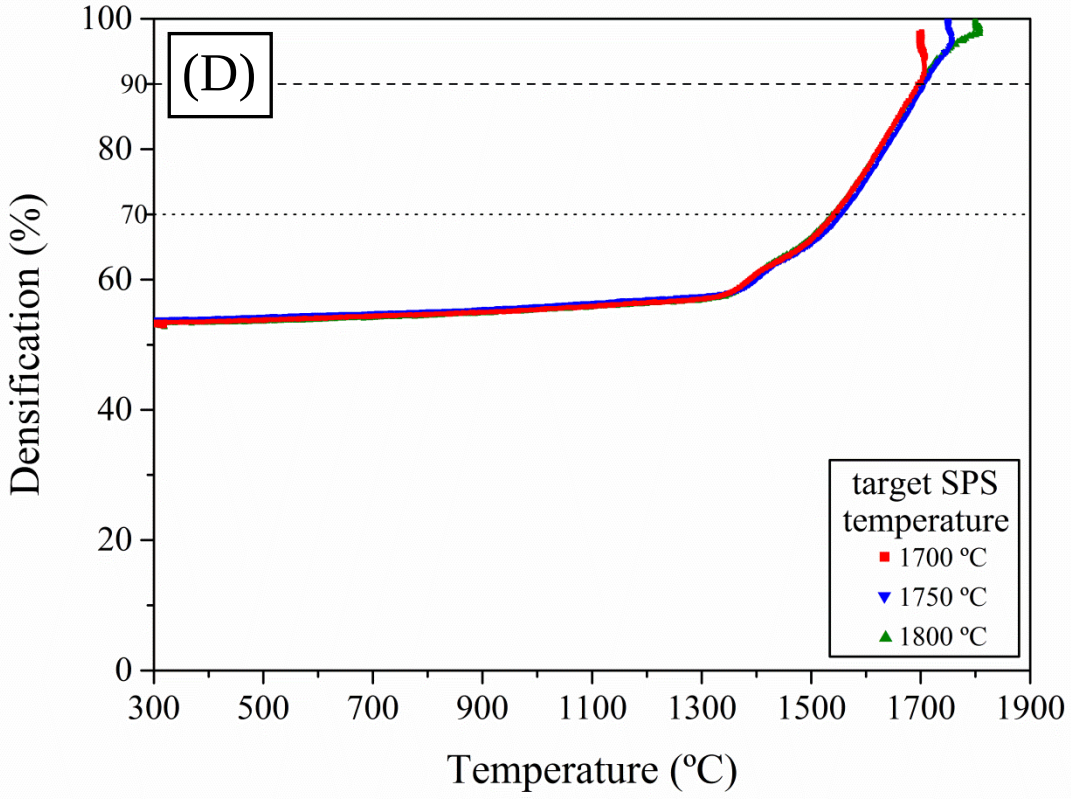

Ojalvo *et al.*
Figure 6

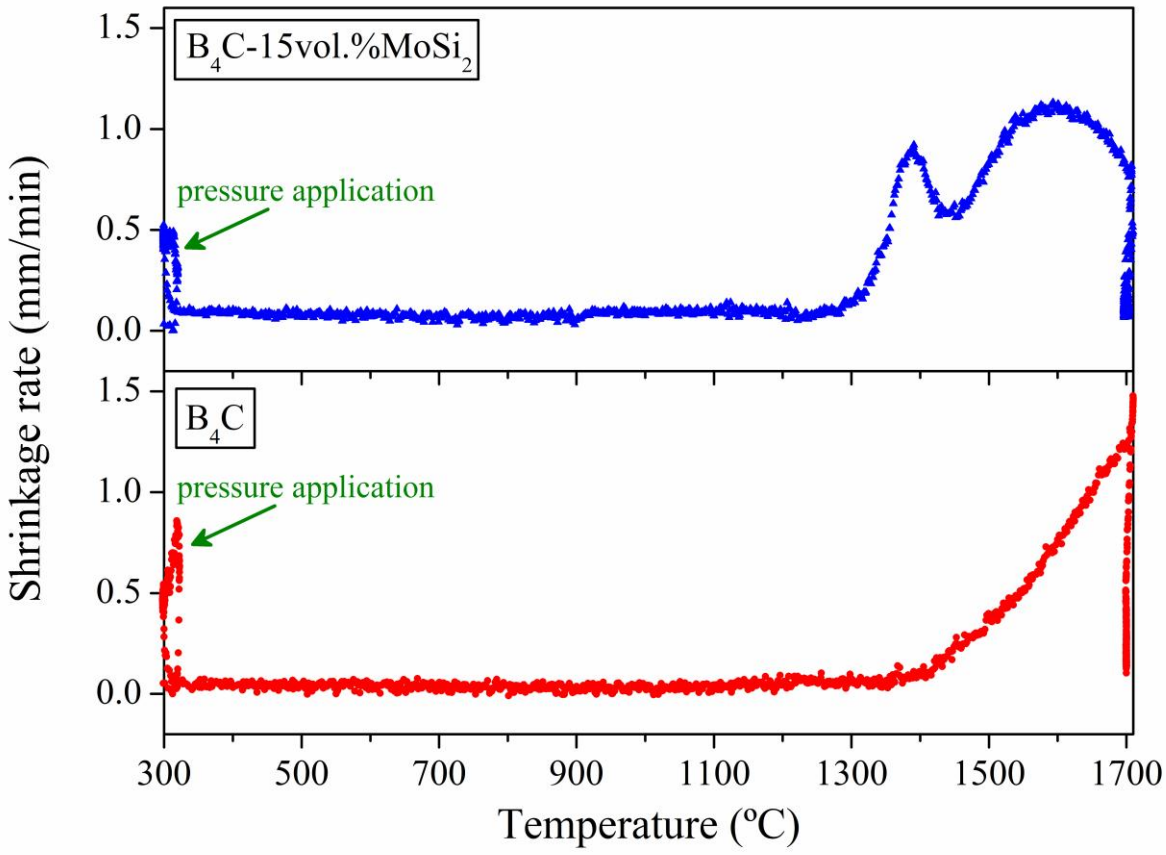

Ojalvo *et al.*
Figure 7

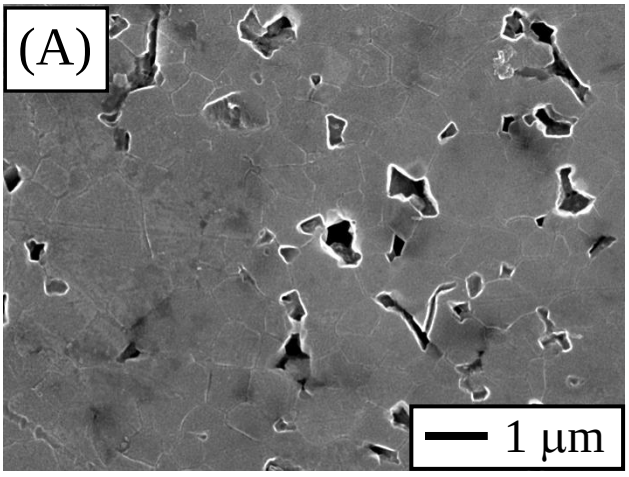

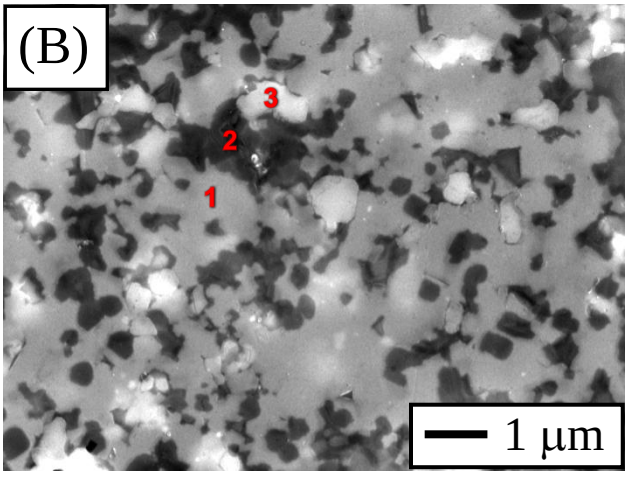

Ojalvo *et al.*
Figure 8

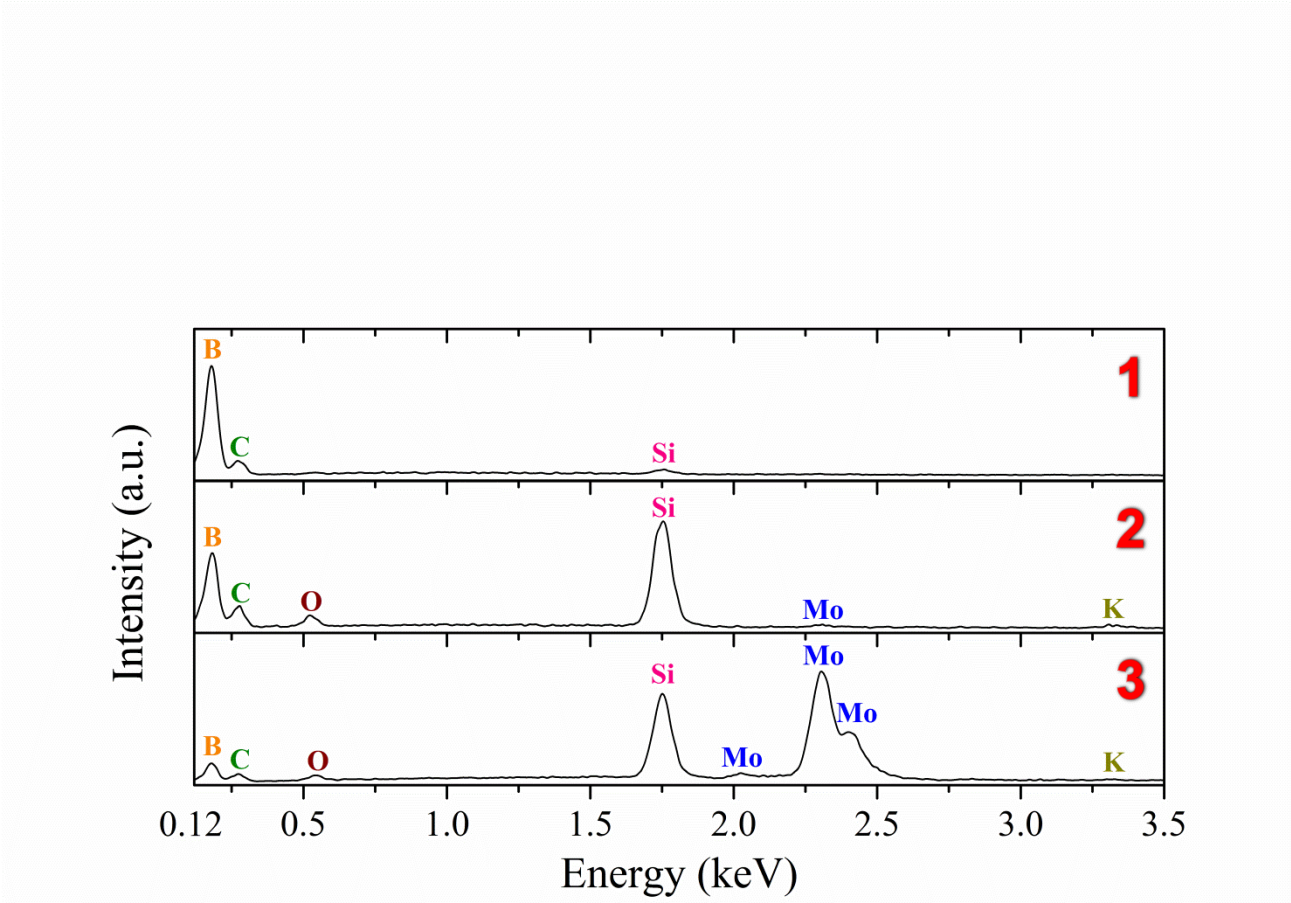

Ojalvo *et al.*
Figure 9

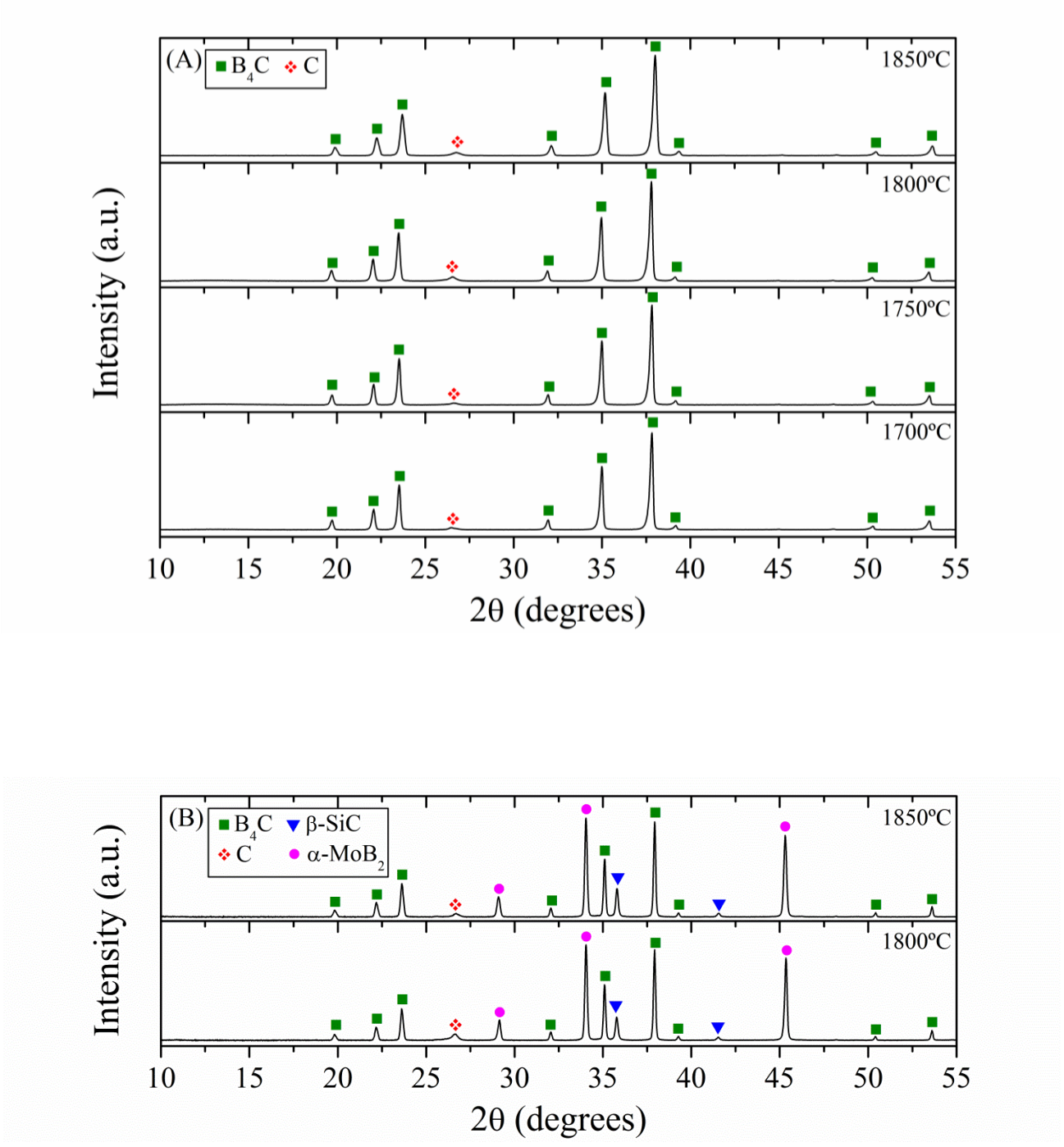

Ojalvo *et al.*
Figure 10

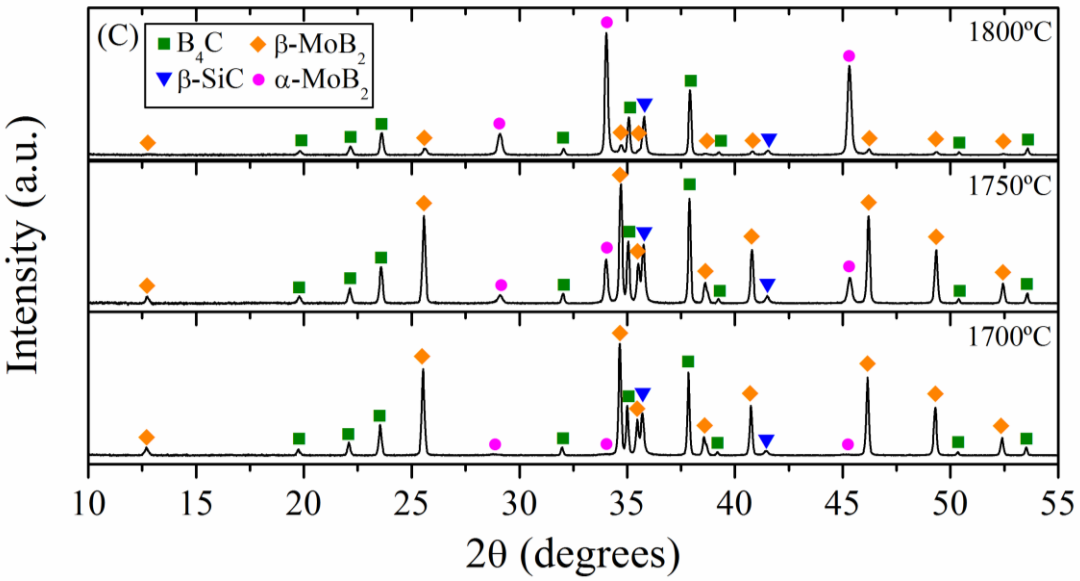

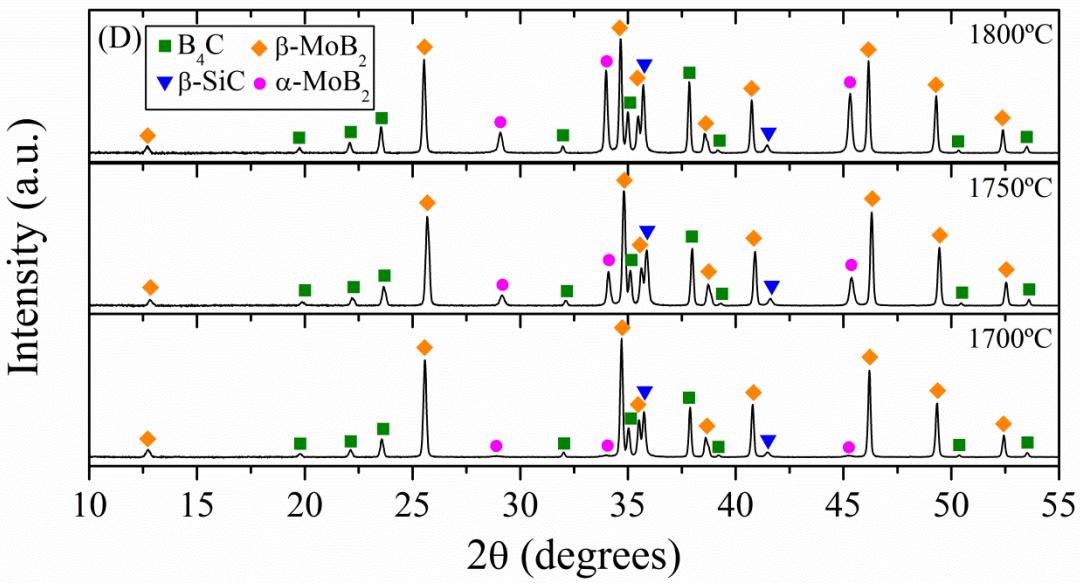

Ojalvo *et al.*
Figure 10

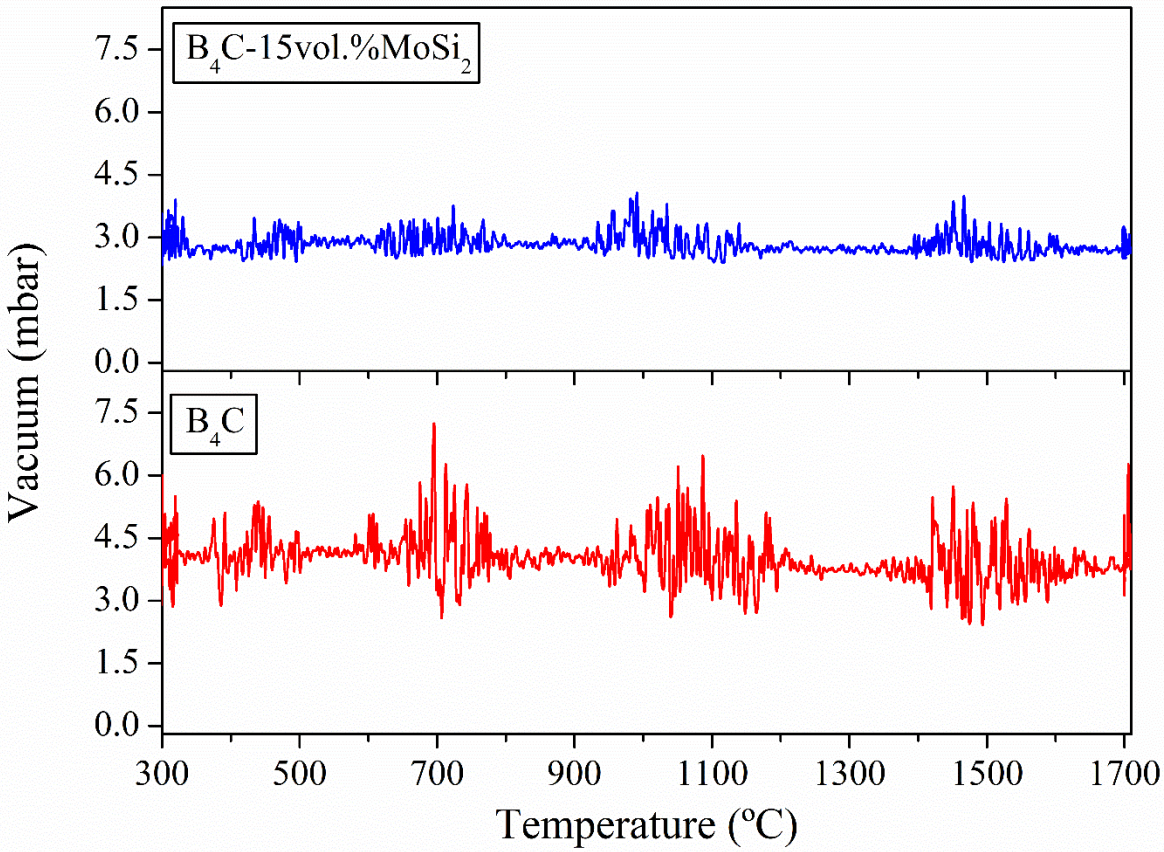

Ojalvo *et al.*
Figure 11

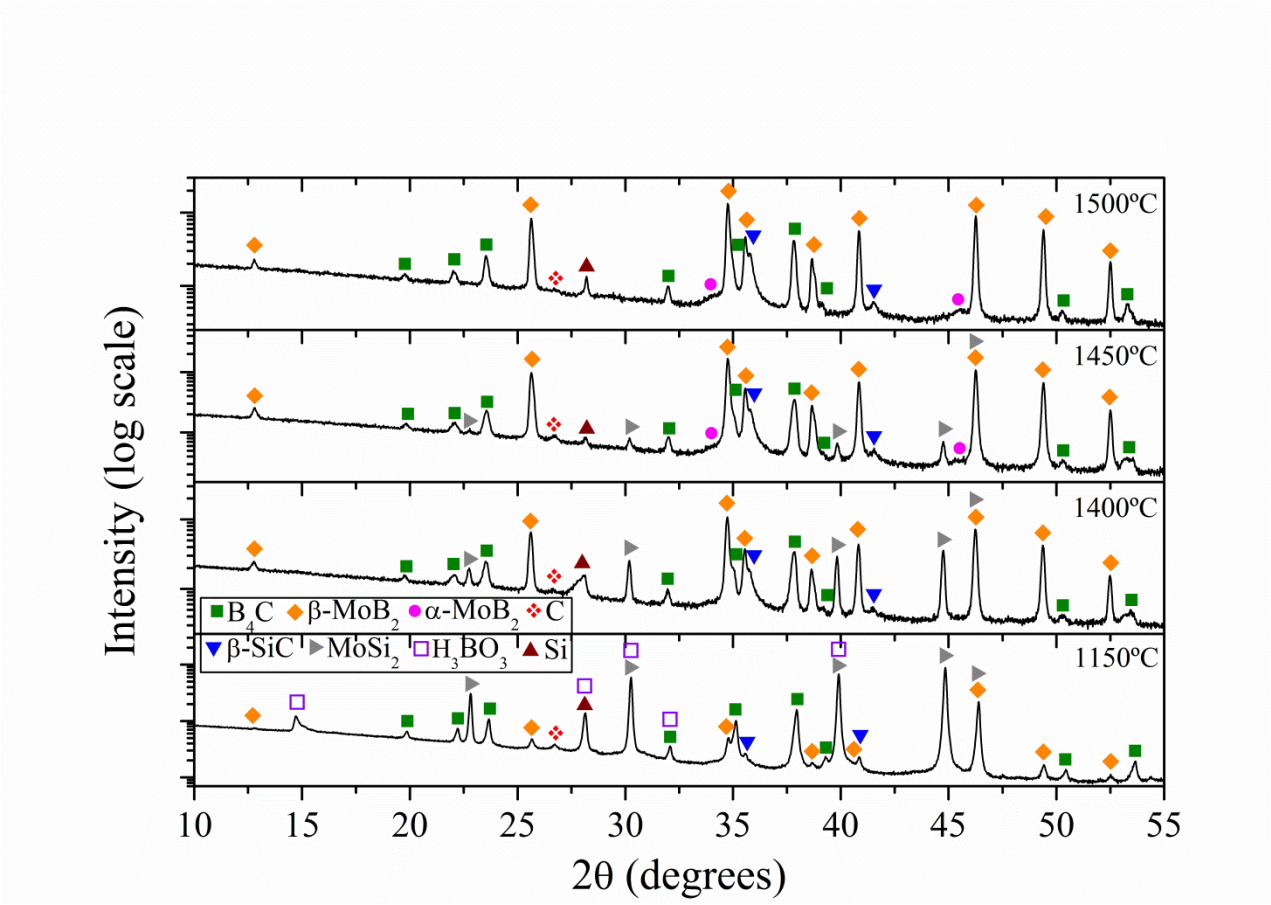

Ojalvo *et al.*
Figure 12

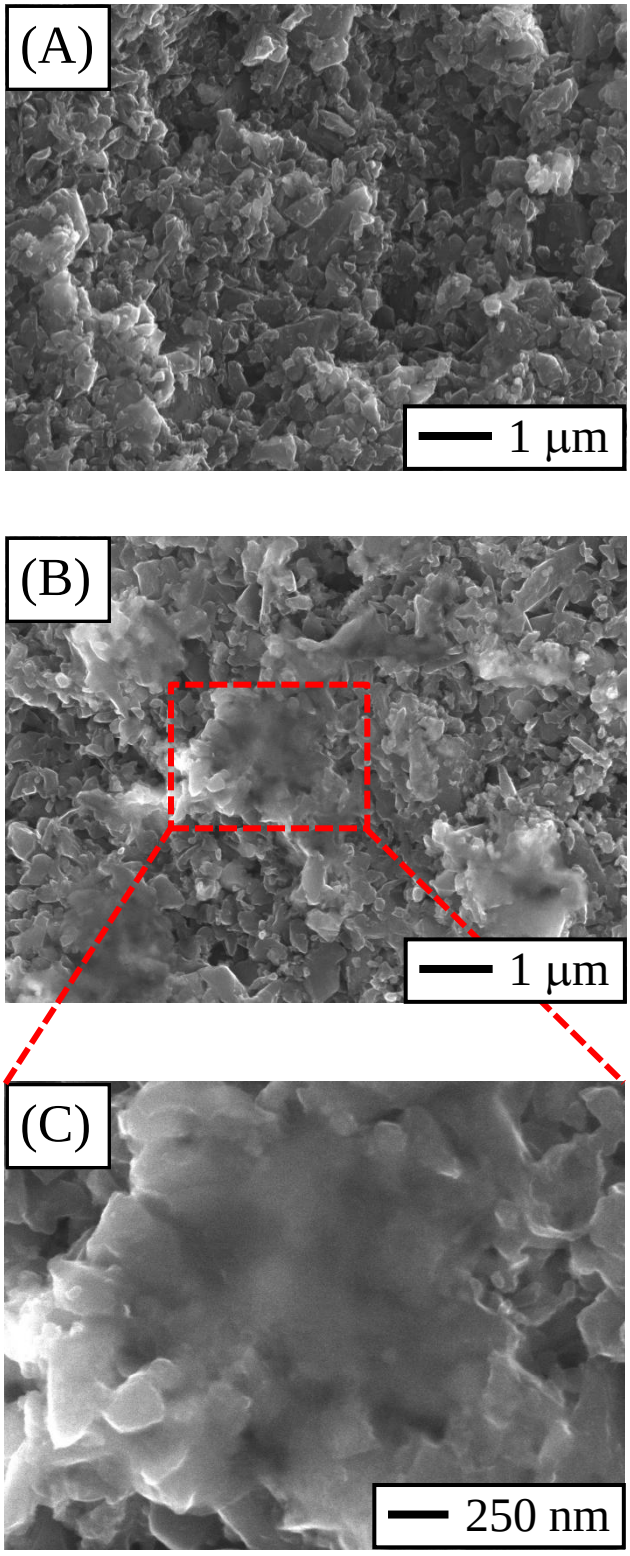

Ojalvo *et al.*
Figure 13

Figure Captions

Figure 1. Representative SEM micrographs of the fracture surface of the monolithic B_4C ceramics fabricated by SPS using target temperatures of (A) 1700, (B) 1750, (C) 1800, and (D) 1850 °C.

Figure 2. Representative SEM micrographs of the fracture surface of the B_4C composites fabricated by SPS using 5 vol.% $MoSi_2$ sintering additive and target temperatures of (A) 1800 and (B) 1850 °C.

Figure 3. Representative SEM micrographs of the fracture surface of the B_4C composites fabricated by SPS using 10 vol.% $MoSi_2$ sintering additive and target temperatures of (A) 1700, (B) 1750, and (C) 1800 °C.

Figure 4. Representative SEM micrographs of the fracture surface of the B_4C composites fabricated by SPS using 15 vol.% $MoSi_2$ sintering additive and target temperatures of (A) 1700, (B) 1750, and (C) 1800 °C.

Figure 5. (A) Representative SEM micrograph of the fracture surface of the B_4C composite fabricated by SPS using 15 vol.% $MoSi_2$ sintering additive and a target temperature of 1750 °C, and the corresponding elemental compositional maps of (B) Mo and (C) Si obtained by EDS.

Figure 6. Densification curves as a function of temperature for (A) the B_4C powder, and for the B_4C-$MoSi_2$ powder mixtures with (B) 5, (C) 10, and (D) 15 vol.% $MoSi_2$ logged during their SPS cycles with different target temperatures. The degrees of densification corresponding to the

onset of the intermediate (70%) and final (90%) stages of sintering are marked by dotted and dashed lines, respectively.

Figure 7. Shrinkage-rate curve as a function of temperature for the B_4C powder and for the B_4C-$MoSi_2$ powder mixture with 15 vol.% $MoSi_2$ logged during their SPS cycle with a target temperature of 1700 °C.

Figure 8. Representative SEM micrographs of the electrochemically-etched, polished surface of (A) the monolithic B_4C ceramic and (B) the B_4C composite with 15 vol.% $MoSi_2$ sintering additive fabricated by SPS using a target temperature of 1800 °C.

Figure 9. EDS spectra corresponding to the locations indicated by the numbers in Fig. 8B. Peak assignations are included. K and O come from the electrochemical etching with KOH solution. Si detected in 1, B and Mo detected in 2, and Si and C detected in 3 come from neighbouring grains because the effective interaction volume is larger than grain size.

Figure 10. XRD patterns of (A) the monolithic B_4C ceramics and of the B_4C composites with (B) 5, (C) 10, and (D) 15 vol.% $MoSi_2$ sintering additives fabricated by SPS using different target temperatures. Peak assignations are included.

Figure 11. Evolution of the vacuum level within the chamber of the SPS furnace as a function of temperature for the B_4C powder and for the B_4C-$MoSi_2$ powder mixture with 15 vol.% $MoSi_2$ logged during their SPS cycle with a target temperature of 1700 °C.

Figure 12. XRD patterns of the B_4C composites fabricated by SPS using 15 vol.% $MoSi_2$ sintering additive and cycles interrupted at 1150, 1400, 1450, and 1500 °C. Peak assignations are included. Logarithmic scales have been used to facilitate the observation of the weaker XRD peaks.

Figure 13. Representative SEM micrographs of the fracture surface of the B_4C composite with 15 vol.% $MoSi_2$ sintering additive fabricated by SPS using a cycle interrupted at (A) 1250 and (B) 1400 °C. (C) SEM micrograph at higher magnification of a region in (B), showing more detail.

Tables

Table 1. Fabrication conditions of all monolithic ceramics and ceramic composites, and their corresponding degrees of densification.

Type [&]	Target SPS temperature (°C) [#]			
	1700	**1750**	**1800**	**1850**
B_4C	✓ extremely porous	✓ very porous	✓ porous	✓ near-fully dense
B_4C-5vol.%$MoSi_2$	—	—	✓ near-fully dense	✓ fully dense
B_4C-10vol.%$MoSi_2$	✓ porous	✓ near-fully dense	✓ fully dense	—
B_4C-15vol.%$MoSi_2$	✓ near-fully dense	✓ fully dense	✓ fully dense	—

[&] Designations refer to the composition of the powder batches. [#] Other SPS conditions were: heating ramp of 100 °C/min and soaking time of 5 min at the target temperature. The lowest target SPS temperatures required to achieve near-full and full densification are in blue and red, respectively. The following five ranges of densification (d) have been defined: Full dense (d=100%), near-full dense (95≤d<100%), porous (90≤d<95%), very porous (80≤d< 90%), and extremely porous (d<80%).

Table 2. Fabrication conditions, degrees of densification achieved, and mechanical properties of the monolithic ceramics and ceramic composites.

Type [&]	Target SPS temperature (°C) [#]	Densification (%)	Hardness (GPa)	Fracture toughness (MPa·m $^{1/2}$)
B_4C	1700	78	13±1	—
	1750	82	14±1	—
	1800	93	19±1	—
	1850	95	25.0±0.7	—
B_4C-5vol.%$MoSi_2$	1800	96	19.8±0.8	—
	1850	100	29.5±0.9	3.1±0.2
B_4C-10vol.%$MoSi_2$	1700	93	15.0±0.5	—
	1750	96	20±1	—
	1800	100	30.1±0.9	3.7±0.3
B_4C-15vol.%$MoSi_2$	1700	97.5	23±1	—
	1750	100	30.1±0.7	4.1±0.3
	1800	100	30.1±0.6	4.1±0.3

[&] Designations refer to the composition of the powder batches. [#] Other SPS conditions were: heating ramp of 100 °C/min and soaking time of 5 min at the target temperature.

***Summary of Novel Conclusions**

- Toughened, super-hard B_4C triplex-particulate composites have been fabricated at lower than usual temperatures by spark plasma sintering with $MoSi_2$ additives (5, 10, and 15 vol.%).
- It is proved that $MoSi_2$ is a reactive sintering additive that promotes densification by transient liquid-phase sintering, thus yielding fully-dense B_4C-MoB_2-SiC composites at relatively lower temperatures.
- It is demonstrated that the $MoSi_2$ first reacts at moderate temperatures with part of B_4C to form MoB_2, SiC, and Si. This last is a transient component that eventually melts, contributing to densification by liquid-phase sintering, and then reacts with free C present in the B_4C starting powders to form more SiC, after which densification continues by solid-state sintering.
- It is shown that that the B_4C-MoB_2-SiC composites are super-hard (~30 GPa), tough (~3-4 $MPa{\cdot}m^{1/2}$), and fine-grained, a combination that renders them very appealing for structural applications.
- Research opportunities are discussed for the future microstructural design of a novel family of toughened, ultra-hard/super-hard multi-particulate composites based on B_4C plus refractory borides and carbides.